Waves in Random and Complex Media

https://www.tandfonline.com/journals/twrm20

Accepted December 27th 2021

Numerical investigation on transient third-grade magnetized nanofluid flow and radiative convection heat transfer from a stationary/moving cylinder: Nanomaterial and nanoparticle shape effects

Ashwini Hiremath[1], G. Janardhana Reddy[1,*], O. Anwar Bég[2] and Harish Holla[3]

[1]Department of Mathematics, Central University of Karnataka, Kalaburagi, ***India****.*

[2]Professor and Director- Multi-physical Engineering Sciences, Aeronautical and Mechanical Engineering Department, School of Science, Engineering and Environnment, University of Salford, Manchester M54WT, ***UK.***

[3]Department of Chemistry, Central University of Karnataka, Kalaburagi, ***India****.*

[*]Corresponding author- Email: **gjr@cuk.ac.in**

ABSTRACT

In this study, a mathematical model is developed for analyzing the time-dependent magneto-convective flow and heat transfer characteristics of an electrically conducting (functional) third-grade Reiner-Rivlin non-Newtonian nanofluid from a moving or stationary hot cylinder in the presence of magnetic field and thermal radiation. A well-tested convergent Crank-Nicolson type finite difference algorithm is employed to solve the transformed, nonlinear boundary value problem. The Tiwari-Das nanofluid volume fraction model is adopted for nanoscale effects and the Rosseland algebraic flux model for radiative heat flux effects. It has been shown that the shape of nanoparticles remarkably contributes to the enhancement of heat transfer. Several metallic nanoparticle types such as Al_2O_3, *Cu*, and TiO_2 are examined. It is found from the investigation that the viscoelastic nanofluid with TiO_2 nanoparticles results in more heat transfer than the other nanoparticles. Lower velocity and higher temperature values are computed at transient conditions with a higher third-grade fluid parameter for the flow of nanofluid (Al_2O_3-*SA*). The plots of transient friction and heat transfer coefficients are visualized at the surface of a hot cylinder. The tabulated heat transfer coefficient is comparatively more for the moving cylinder than the stationary cylinder. Detailed validation of results of the numerical scheme with previous studies is included. The simulations find applications in coating deposition (enrobing) of magnetic nanomaterial at high temperatures, functional nanomaterial synthesis, etc.

KEYWORDS: *Unsteady MHD Non-Newtonian nanofluid flow, Vertical Cylinder, Convection and Radiation, Numerical, Functional coating.*

NOMENCLATURE

A volume fraction function

Al_2O_3 Alumina

B volume fraction function

Cu Copper

C volume fraction function

C_p specific heat at constant pressure

$\overline{C_f}$ dimensionless average momentum transport coefficient

D volume fraction function

$\frac{d}{dt}$ material time derivative

E thermal conductivity ratio (nanofluid to base fluid)

g′ acceleration due to gravity

Gr Grashof number

I identity tensor

k thermal conductivity

M magnetic body force parameter

Nr conduction-radiation parameter

$\overline{Nu}$ average heat transport coefficient

P fluid pressure

Pr Prandtl number

q_r radiative heat flux

r radial coordinate

r_o radius of the cylinder

R dimensionless radial coordinate

S_1', S_2', S_3' Rivlin and Ericksen stress tensors

tr trace

t dimensionless time

t' time

TiO_2 Titanium oxide

T' temperature

T dimensionless temperature

T^{**} matrix transposition

x axial coordinate

X dimensionless axial coordinate

u, v velocity components in (x, r) coordinate system

U, V dimensionless velocity components in X, R directions, respectively

Greek letters

$\alpha_1', \alpha_2', \beta_1', \beta_2', \beta_3'$ rheological material moduli

β_T volumetric thermal expansion coefficient

σ electrical conductivity

β non-dimensional third-grade fluid parameter

τ' Cauchy stress tensor

ρ density

φ volume fraction of nanoparticles

μ dynamic viscosity

ϑ kinematic viscosity

σ^* Stefan-Boltzmann constant

κ^* mean absorption coefficient

Subscripts

f, g grid levels in (X, R) coordinate system

nf nanofluids

bf base fluid

s solid nanoparticles

w wall conditions

∞ ambient conditions

Superscripts

h time level

1. INTRODUCTION

The science of nanomaterials has emerged as a significant area in 21st-century technology. The synthesis of nanomaterials takes place at the nanoscale and these nano-sized materials may be in the form of films, tubes, wires, rods, shells, fibers, polymeric structures, spherical particles, and many other shapes. The colloidal mixture of these nanomaterials in the regular base fluid (which has weaker thermophysical properties such as thermal conductivity) has furnished a new class of functional fluids called '*nanofluids'* (with improved thermophysical characteristics such as thermal diffusivity and conductivity, viscosity, and coefficient of convective heat transfer, etc.). The strategic deployment of these nanomaterials (i.e., nanofluids) has witnessed remarkable success in many heat transfer applications like industrial heating/cooling appliances, industrial transportation, heat exchangers, solar collectors, nuclear power plants, granular and fiber thermal insulation, petroleum displacement liquids, catalytic reactors, aircraft wing coatings, marine anti-fouling, and anti-corrosion coatings, etc. Yet, further applications are emerging in biomedical engineering and include drug delivery, wound healing, tissue regeneration, biomagnetic nano-pharmacodynamics, etc. The nanoparticle geometrical shape (spherical, cylindrical, or other), size (in nanometers), and volume fraction (i. e. percentage doping) in the base fluid are key factors controlling the efficacy of thermo-physical behavior of the nanofluid. Masuda *et al.* [1] verified an increment in thermal efficiency by introducing ultra-fine solid particles in a regular fluid, utilizing solid metallic particles, and confirming a substantial increase in thermal conductivity. They demonstrated that particles of the smallest size (nano) in base fluid with the greatest surface

area are responsible for high rates of heat transfer. Xuan and Li [2] have provided experimental verification for how nanoparticle volume fraction accounts for amplified thermal conductivity. Putra *et al.* [3] have examined how different types of material (metallic or non-metallic or some oxides) and concentration of particles (nano-sized) enhance the thermal performance of nanofluids. Timofeeva *et al.* [4] also confirmed the effect of size (in nanoscale) of particles on the elevation in global thermal conductivity. The stability of nanofluids is also critical for their efficiency during implementation in different systems and has been examined rigorously by Yu and Xie [5].

The above review of literature on nanofluids is largely confined to Newtonian behavior (linear relation of stress and strain). Nevertheless, there are numerous distinctive rheological characteristics exhibited by nanofluids which confirm the non-linear relationship of stress and stain such as relaxation of stress, non-linearity of creeping, threshold stress, normal stress differences, variation in viscosity, shear thickening/thinning, temperature-dependent viscosity, and memory. These typical behaviors are inefficiently explained by the classical viscous (Navier-Stokes) model. There are many experimental results which have proven that nanofluids show strong non-Newtonian behavior. These characteristics may be attributable to the addition of nanoparticles to the base fluid (which modifies the rheology) or indeed be associated with the base fluid itself prior to doping with nanoparticles (e. g. polymeric coating base fluids). Tseng and Chen [6] experimentally investigated the pseudoplastic (shear-thinning) flow of suspensions of nickel-terpineol. Tseng and Lin [7] deployed a variety of viscoplastic ("yield stress") rheological models such as the Casson, Bingham, and Herschel-Bulkley models to determine the yield stress of suspensions of titanium oxide under different shear rates. Kathy Lu [8] showed experimentally that nanofluids comprising Al_2O_3 and CNT- Al_2O_3 (CNT-carbon nanotube) exhibit shear-thinning properties with variation in the shear rate. Chen *et al.* [9] demonstrated the concentration and temperature dependent rheology of nanofluids. Phuoc and Massoudi [10] have reported that nanofluids exhibit yield stress and behave as a viscoplastic non-Newtonian fluid. Chen *et al.* [11]

have given experimental results on temperature and concentration dependent non-Newtonian nanofluid behavior and have furthermore validated their results theoretically. Hojjat *et al.* [12] observed the non-Newtonian behavior of nanofluid by taking the base fluid as non-Newtonian fluid with 0.5 wt. % aqueous solution of carboxymethyl cellulose. Kole and Dey [13] showed that the addition of nanoparticles to base fluids generates significant non-Newtonian behavior of the resulting nanofluid. Non-Newtonian nanofluid mechanics provides a more refined model for real nanoliquids compared with conventional Newtonian nanofluids, and as such enables a more realistic assessment of actual industrial systems including the melting of nano-polymers, nano-doped biological liquids (e. g. blood, synovial fluid), coatings, adhesives, paints etc.

For simulation of thermofluid dynamics behaviour of real nanofluids, it is essential to consider suitable '*non-Newtonian theory*' combined with an appropriate '*nanoscale model*'. There are many efficient rheological models (rate type, integral type, and differential type) to explain the non-linear behavior of stress-strain in nanofluids. These include the micropolar model [14], second-order viscoelastic model [15], Williamson model [16], Reynolds exponential viscosity model [17] Ostwald-DeWaele power-law model [18]. The fluid models of *differential type* (i.e., models of the Reiner-Rivlin family) are primarily concerned with characterizing polymer flows which are known to exhibit a complex relationship between the stress history and deformation gradient. One of the differential types with high non-linearity of stress and strain is the *third-grade fluid* model. This class of fluid is characterized by shear thinning (inverse relationship of shear viscosity and shear rate) or shear thickening (direct relationship of shear viscosity and shear rate) and quite accurately captures the rheological behaviour of real viscoelastic polymers [19], [20]. Of course, there are other alternative constitutive viscoelastic models including the second-order model, Oldroyd-B, Walters-B short memory model, FENE-P model, Johnson-Segalman model, or the upper convected Maxwell (UCM) model. However, many of these models are special cases of the more general third-grade fluid model which features stress relaxation and retardation effects. In addition, the third-grade model satisfactorily explains fluid such as slurries, biological liquids,

certain coolants, lubricants, and of course polymeric coatings. Many excellent studies have been communicated on convective heat transfer of third-grade fluid flows [21-27]. There have also appeared a number of interesting works which have scrutinized third-grade rheological nanofluid flows. Hiremath *et al*. [28] investigated the third-grade nanofluid flow from a convectively heated vertical cylinder and examined heat transfer characteristics for different material parameter effects. The dissipative two-layer buoyancy-driven channel flow of third-grade nanofluid was simulated by Farooq *et al.* [29]. Nadeem and Saleem [30] have considered the spin boundary layer flow of a third-grade nanofluid on a vertical revolving cone geometry. Khan *et al*. [31] have deployed shooting and finite difference techniques for computing steady-state boundary layer convective flows of third-grade nanofluid. Qayyum *et al.* [32] have employed the third-grade viscoelastic model to investigate hydromagnetic radiative nanofluid flows with thermophoresis and Brownian motion under Newtonian heating conditions. Hayat *et al.* [33] have employed the homotopy analysis method to compute third-grade nanofluid boundary layer flows with heat source and chemical reaction effects. All these studies clearly show the deviation of thermal flow and heat transfer characteristics of non-Newtonian viscoelastic third-grade nanofluid from results computed with the simpler Newtonian fluid model.

The current work aims to explore numerically *the enhancement in heat transfer by adding nanoparticles to magnetohydrodynamic viscoelastic polymer coating flow on a stationary/moving cylinder under a radial magnetic field*. The present research article describes in detail the numerical computation of this functional nanopolymeric coating flow regime, based on an unconditionally stable implicit finite difference scheme. This enables the determination of the effect of volume fraction on *functional* non-Newtonian nanofluids flow over a moving vertical cylinder, a problem which has been explored without complex rheology or a variety of different nanoparticles in [34], [35] & [36]. Three metallic nanoparticles i.e. Al_2O_3, *Cu, and* TiO_2 are studied to compute the relative heat transfer characteristics. The Tiwari-Das nanoscale and Rosseland radiative flux models are deployed. In particular, the considered flow is time-dependent free

convective laminar boundary layer flow. The present flow model considers a specific example of third-grade non-Newtonian fluid as Sodium Alginate (*SA*). Many authors have already used SA as a non-Newtonian fluid [37-42]. Alumina (Al_2O_3), Copper (*Cu*), and Titanium oxide (TiO_2) are the nanoparticles and Sodium Alginate (*SA*) is the base fluid. The steady and unsteady flow variables, heat transfer coefficient, and skin friction are computed with appropriate initial and boundary conditions using the implicit Crank-Nicolson numerical scheme. Further, the thermal nano-coating has advantages as it provides high thermal conductivity, durability and sustainability (it can call "greener"). Also, it is hydrophobic by nature offers least surface energy and greater surface area. The thermal performance of many industrial and automobile components such as blades of gas turbine, heat exchangers, and landing gear components of aerospace can be improved with the help of thermal nano-coating which enhance wear resistance and dissipates heating. Furthermore, it can lengthen the life components via mitigation of oxidation, abrasion, corrosion, and swarfing. Nano-coatings even can improve the hydrophobicity to the surface of geometry which is in contact with fluid by enhancing heat transfer performance with minimum frictional energy losses. Therefore, thermal nano-coatings have significant applications in coating, tribological, and sustainable features to working geometrical surfaces. Finally, the application of this research work is in high temperature *thermal nano-coating, polymer and fabrication technology*. The present study has thus far not appeared in the scientific literature.

2. MAGNETIC NANOFLUID THIRD-GRADE VISCOELASTIC FLOW MODEL

The current study examines the electrically conducting viscoelastic third-grade nanofluid over a semi-infinite moving (or stationary) cylinder (radius r_0) which is directed vertically under static, transverse radial magnetic field M_0 (depicted in **Fig. 1)**. Electromagnetic induction and Ohmic dissipation effects are negated. Axial (x-axis) and radial (r-axis) coordinates are taken into account to describe the flow-domain, where the x-axis is positioned along the cylinder and the r-axis is oriented in the direction normal to the cylinder. At the beginning of flow (i.e., at $t' = 0$), both solid

(cylinder) and fluid (third-grade nanofluid) maintain the common temperature T'_∞. The cylinder starts moving in the axial direction (translation) with constant velocity u_0 for $t' > 0$. At the same time, a temperature gradient (temperature difference) is introduced, so as to increase the cylinder surface temperature to T'_w. With further advancement in time, a constant temperature is preserved i. e. isothermal conditions are achieved. The non-Newtonian third-grade (*SA*- Sodium Alginate) based nanofluid contains different kinds of nanoparticles such as TiO_2, *Cu*, and Al_2O_3.

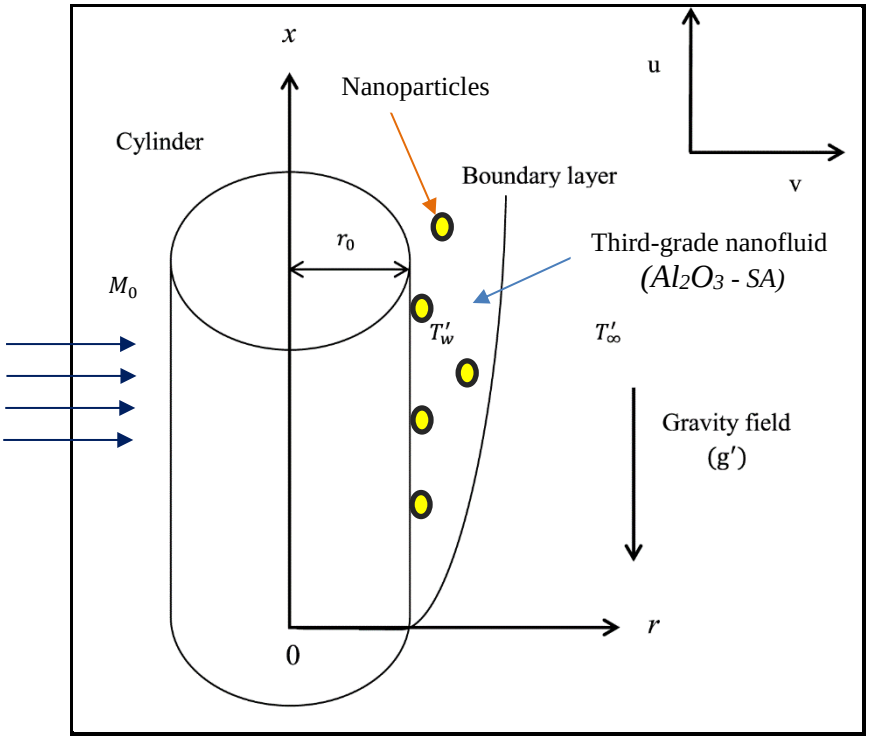

Fig. 1. Physical description of coating flow of magnetic nano-polymer over a cylinder.

The considered nanofluids in the current study are simulated as a single-phase fluid system. Also, the establishment of local thermal equilibrium between the nanoparticles and third-grade fluid is necessary to satisfy the no-slip condition. The thermophysical conditions of the nanoparticles & base fluid are listed in **Table 1.**

2.1 Description of the non-Newtonian fluid (third-grade fluid) model with constitutive relation:

Equation (1) presents the "Cauchy's stress-tensor (τ')" for the viscoelastic third-grade fluid having compatible relations thermodynamically (Fosdick and Rajagopal [19]):

$$\tau' = -PI + \mu S_1' + \alpha_1' S_2' + \alpha_2' {S_1'}^2 + \beta_1' S_3' + \beta_2' (S_1' S_2' + S_2' S_1') + \beta_3' (tr{S_1'}^2) S_1' \quad (1)$$

Here, α_l' $(l = 1,2)$ and β_l' $(l = 1,2,3)$ are *temperature-dependent* material components, $-PI$ denotes the spherical portion of τ'(stress-tensor), and S_l' $(l = 1,2,3)$ are 'Rivlin-Ericksen tensor matrices' represented through Eq. (2):

$$S_1' = (\nabla \boldsymbol{V})^{T^{**}} + \nabla \boldsymbol{V} \ , S_l' = \frac{dS_{l-1}'}{dt} + (\nabla \boldsymbol{V})^{T^{**}} S_{l-1}' + S_{l-1}' (\nabla \boldsymbol{V}), \ \ l = 2,3 \ldots. \quad (2)$$

The transpose of matrix, gradient operator, velocity vector are symbolized as T^{**}, ∇, $\boldsymbol{V}$ respectively. $\frac{d}{dt}$ designates the material derivative where $\frac{d}{dt}(\cdot) = \left(\frac{\partial}{\partial t} + \boldsymbol{V}\nabla\right)(\cdot)$. The inequality described by '*Clausius-Duhem*' and the least possible value of '*Helmholtz free-energy*' at the condition of equilibrium are the minimum criteria to be satisfied by the current fluid model (viscoelastic third-grade fluid). Hence, third-grade fluid requires the following restrictions.

$$\mu \geq 0; \quad \alpha_1' \geq 0; \quad |\alpha_1' + \alpha_2'| \leq \sqrt{24\mu\beta_3'} \quad (3.a)$$

$$\beta_1' = 0; \quad \beta_2' = 0; \quad \beta_3' \geq 0 \quad (3.b)$$

Substitution in Eqn. (1), leads to:

$$\tau' = -PI + \mu S_1' + \alpha_1' S_2' + \alpha_2' {S_1'}^2 + \beta_3' (tr{S_1'}^2) S_1' \quad (4)$$

Further, boundedness criteria, stability and fluid thermodynamics, studies are similarly explained as the second-grade fluid model (investigated by Dunn and Fosdick [55], for $\beta_3' = 0$, constitutive relation reduces to second-grade fluid model). Fosdick and Straughan [56] revealed that the non-physical results are observed for $\alpha_1' < 0$ & asymptotic stability criteria for $\alpha_1' \geq 0$.

The considered flow model is axisymmetric. This axisymmetric thermal convective flow of a viscoelastic third grade nanofluid in the presence of '*transverse radial magnetic field* (M_0)' from the moving cylinder (velocity u_0) is characterized by the subsequent 'momentum' and 'energy'

equations [43] including Boussinesq's approximation [44] in the occurrence of thermal radiative flux are presented as [23], [27], [28], [36]:

$$\frac{\partial(ru)}{\partial x}+\frac{\partial(rv)}{\partial r}=0 \tag{5}$$

The considered cylindrical geometry is under the influence of a transverse magnetic field of intensity M_0 as described in **Fig. 1**. The *magnetic Reynolds number* is presumed to be very small, therefore the interaction of the induced magnetic field in the axial direction with the flow of the third-grade nanofluid (which is electrically conducting) can be ignored i.e. magnetic field is not distorted.

$$\frac{\partial u}{\partial t'}+v\frac{\partial u}{\partial r}+u\frac{\partial u}{\partial x}=\frac{(\rho\beta)_{nf}}{\rho_{nf}}\mathrm{g}'(T'-T'_{\infty})+\vartheta_{nf}\frac{1}{r}\frac{\partial}{\partial r}\left(r\frac{\partial u}{\partial r}\right)+\frac{\alpha'_1}{\rho_{nf}}\left[\frac{\partial^3 u}{\partial r^2\partial t'}+\frac{1}{r}\frac{\partial^2 u}{\partial r\partial t'}+v\frac{\partial^3 u}{\partial r^3}\right.$$

$$+2\frac{\partial v}{\partial r}\frac{\partial^2 u}{\partial r^2}+3\frac{\partial^2 u}{\partial r^2}\frac{\partial u}{\partial x}+\frac{\partial u}{\partial r}\frac{\partial^2 v}{\partial r^2}+4\frac{\partial u}{\partial r}\frac{\partial^2 u}{\partial x\partial r}+\frac{v}{r}\frac{\partial^2 u}{\partial r^2}+\frac{u}{r}\frac{\partial^2 u}{\partial x\partial r}+$$

$$\left.\frac{3}{r}\frac{\partial u}{\partial x}\frac{\partial u}{\partial r}+u\frac{\partial^3 u}{\partial x\partial r^2}+\frac{1}{r}\frac{\partial u}{\partial r}\frac{\partial v}{\partial r}\right]+\frac{\alpha'_2}{\rho_{nf}}\left[\frac{2}{r}\frac{\partial u}{\partial r}\frac{\partial v}{\partial r}+\frac{2}{r}\frac{\partial u}{\partial x}\frac{\partial u}{\partial r}+2\frac{\partial^2 u}{\partial r^2}\frac{\partial u}{\partial x}+\right.$$

$$+2\frac{\partial^2 v}{\partial r^2}\frac{\partial u}{\partial r}+2\frac{\partial v}{\partial r}\frac{\partial^2 u}{\partial r^2}+4\frac{\partial u}{\partial r}\frac{\partial^2 u}{\partial x\partial r}\Big]+\frac{\beta'_3}{\rho_{nf}}\left[\frac{2}{r}\left(\frac{\partial u}{\partial r}\right)^3+6\left(\frac{\partial u}{\partial r}\right)^2\frac{\partial^2 u}{\partial r^2}+\right.$$

$$\left.4\left(\frac{\partial u}{\partial r}\right)^2\frac{\partial^2 u}{\partial x^2}+2\frac{\partial u}{\partial x}\frac{\partial u}{\partial r}\frac{\partial^2 u}{\partial x\partial r}\right]-\frac{\sigma M_0^2 u}{\rho_{nf}} \tag{6}$$

where, (u, v) denotes the components of velocity in the (x, r) directions.

$$\frac{\partial T'}{\partial t'}+u\frac{\partial T'}{\partial x}+v\frac{\partial T'}{\partial r}=\frac{k_{nf}}{(\rho C_p)_{nf}}\frac{1}{r}\frac{\partial}{\partial r}\left(r\frac{\partial T'}{\partial r}\right)-\frac{1}{(\rho C_p)_{nf}}\frac{1}{r}\frac{\partial}{\partial r}(rq_r) \tag{7}$$

The appropriate initial and boundary conditions are imposed as follows:

$$\begin{aligned}
&t'\le 0: \quad T'=T'_{\infty}, \quad v=0, \ u=0 && \text{for all } x \text{ and } r\\
&t'>0: \quad T'=T'_{w}, \quad v=0, \ u=\gamma u_0 && \text{at } r=r_0\\
&\qquad\quad T'=T'_{\infty}, \quad v=0, \ u=0 && \text{at } x=0\\
&\qquad\quad T'\to T'_{\infty}, \quad v\to 0, \ u\to 0, \frac{\partial u}{\partial r}\to 0 && \text{as } r\to\infty
\end{aligned} \tag{8}$$

The density, thermal expansion coefficient, and heat capacitance for the nanofluid are calculated using the functions in the Tiwari-Das nanoscale model:

$$\begin{aligned} \rho_{nf} &= (1-\varphi)\rho_{bf} + \varphi\rho_s \\ (\rho\beta)_{nf} &= (1-\varphi)(\rho\beta)_{bf} + \varphi(\rho\beta)_s \\ \left(\rho C_p\right)_{nf} &= (1-\varphi)\left(\rho C_p\right)_{bf} + \varphi\left(\rho C_p\right)_s \end{aligned} \tag{9}$$

Also, the thermal conductivity of nanofluid is considered via the Hamilton and Crosser model [45] i.e.,

$$\frac{k_{nf}}{k_{bf}} = \frac{k_s+(n-1)k_{bf}-(n-1)\varphi\left(k_{bf}-k_s\right)}{k_s+(n-1)k_{bf}+\varphi\left(k_{bf}-k_s\right)} \tag{10}$$

where, n defines the shape of the nanoparticle. Precisely, $n = 3\ and\ 3/2$ indicate spherical and cylindrical nanoparticles, respectively (refer to **Table. 2**).

By assuming the 'Rosseland's approximation' (Brewster [46]), the radiative heat flux q_r which is directed in the radial (transverse) direction is expressed as,

$$q_r = -\frac{4\sigma^*}{3\kappa^*}\frac{\partial {T'}^4}{\partial r} \tag{11}$$

For adequately smaller temperature differences within the fluid flow ${T'}^4$ may be analyzed as a linear function of the temperature, so that the Taylor series for ${T'}^4$ about T'_∞, after ignoring higher order terms, is specified by:

$${T'}^4 \cong 4T'{T'}_\infty^3 - 3{T'}_\infty^4 \tag{12}$$

By virtue of Eqns. (11) & (12), Eq. (7) emerges as:

$$\frac{\partial T'}{\partial t'} + u\frac{\partial T'}{\partial x} + v\frac{\partial T'}{\partial r} = \frac{k_{nf}}{\left(\rho C_p\right)_{nf}}\frac{1}{r}\frac{\partial}{\partial r}\left(r\frac{\partial T'}{\partial r}\right) + \frac{16\sigma^*{T'}_\infty^3}{3\left(\rho C_p\right)_{nf}\kappa^*}\frac{1}{r}\frac{\partial}{\partial r}\left(r\frac{\partial T'}{\partial r}\right) \tag{13}$$

Invoking the following non-dimensional quantities:

$$X=\frac{x\vartheta_{bf}}{u_0{r_0}^2},\qquad R=\frac{r}{r_0},\qquad U=\frac{u}{u_0},\qquad V=\frac{vr_0}{\vartheta_{bf}},\qquad t=\frac{t'\vartheta_{bf}}{{r_0}^2},$$

$$T=\frac{T'-T'_\infty}{T'_w-T'_\infty},\quad Gr=\frac{g'(\beta_T)_{bf}{r_0}^2(T'_w-T'_\infty)}{u_0\vartheta_{bf}},\quad Pr=\frac{\vartheta_{bf}}{\alpha_{bf}},\quad M=\frac{\sigma M_0^2 r_0^2}{\mu_{bf}},\quad Nr=\frac{k_{bf}\kappa^*}{4\sigma^* T'^3_\infty}$$

$$\alpha_1=\frac{\alpha'_1}{\rho_{bf}{r_0}^2},\qquad \alpha_2=\frac{\alpha'_2}{\rho_{bf}{r_0}^2},\qquad \beta=\frac{\beta'_3 u_0^2}{\rho_{bf}{r_0}^2\vartheta_{bf}},\quad \beta'=\frac{\beta'_3\vartheta_{bf}}{\rho_{bf}{r_0}^4} \tag{14}$$

Implementing Eqn. (14) in the conservation Eqns. (5), (6), (13), and Eqn. (8), hence, the following system of non-dimensional governing equations with boundary conditions is produced:

$$\frac{\partial U}{\partial X}+\frac{\partial V}{\partial R}+\frac{V}{R}=0 \tag{15}$$

$$U\frac{\partial U}{\partial X}+V\frac{\partial U}{\partial R}+\frac{\partial U}{\partial t}=AC(Gr)T+AB\frac{1}{R}\frac{\partial}{\partial R}\left(R\frac{\partial U}{\partial R}\right)+A\alpha_1\left[\frac{\partial^3 U}{\partial R^2\partial t}+\frac{1}{R}\frac{\partial^2 U}{\partial R\partial t}+U\frac{\partial^3 U}{\partial X\partial R^2}+V\frac{\partial^3 U}{\partial R^3}+\right.$$
$$\left.\frac{U}{R}\frac{\partial^2 U}{\partial X\partial R}+\frac{V}{R}\frac{\partial^2 U}{\partial R^2}+2\frac{\partial V}{\partial R}\frac{\partial^2 U}{\partial R^2}+3\frac{\partial^2 U}{\partial R^2}\frac{\partial U}{\partial X}+\frac{\partial U}{\partial R}\frac{\partial^2 V}{\partial R^2}+4\frac{\partial U}{\partial R}\frac{\partial^2 U}{\partial X\partial R}+\frac{1}{R}\frac{\partial U}{\partial R}\frac{\partial V}{\partial R}+\frac{3}{R}\frac{\partial U}{\partial X}\frac{\partial U}{\partial R}\right]$$
$$+A\alpha_2\left[\frac{2}{R}\frac{\partial U}{\partial R}\left(\frac{\partial V}{\partial R}+\frac{\partial U}{\partial X}\right)+2\frac{\partial^2 U}{\partial R^2}\left(\frac{\partial U}{\partial X}+\frac{\partial V}{\partial R}\right)+2\frac{\partial U}{\partial R}\left(\frac{\partial^2 V}{\partial R^2}+2\frac{\partial^2 U}{\partial X\partial R}\right)\right]$$
$$+A\beta\left[\frac{2}{R}\left(\frac{\partial U}{\partial R}\right)^3+6\frac{\partial^2 U}{\partial R^2}\left(\frac{\partial U}{\partial R}\right)^2\right]+A\beta'\left[4\frac{\partial^2 U}{\partial X^2}\left(\frac{\partial U}{\partial R}\right)^2+2\frac{\partial^2 U}{\partial X\partial R}\frac{\partial U}{\partial X}\frac{\partial U}{\partial R}\right]-AMU \tag{16}$$

$$U\frac{\partial T}{\partial X}+V\frac{\partial T}{\partial R}+\frac{\partial T}{\partial t}=\frac{D}{Pr}\left(E+\frac{4}{3Nr}\right)\left(\frac{\partial^2 T}{\partial R^2}+\frac{1}{R}\frac{\partial T}{\partial R}\right) \tag{17}$$

$t\le 0$: $T=0$, $V=0$, $U=0$ for all X and R

$t>0$: $T=1$, $V=0$, $U=\gamma$ at $R=1$

$T=0$, $V=0$, $U=0$ at $X=0$ (18)

$T\to 0$, $V\to 0$, $U\to 0$, $\frac{\partial U}{\partial R}\to 0$ as $R\to\infty$

where,

$$A=\frac{1}{\left[(1-\varphi)+\varphi\frac{\rho_s}{\rho_{bf}}\right]};\qquad B=\frac{1}{(1-\varphi)^{2.5}};\qquad C=\left[(1-\varphi)+\varphi\frac{(\rho\beta)_s}{(\rho\beta)_{bf}}\right];$$

$$D = \frac{1}{\left[(1-\varphi)+\varphi\frac{(\rho C_p)_s}{(\rho C_p)_{bf}}\right]} \; ; \qquad E = \frac{k_{nf}}{k_{bf}}$$

(19)

3. FINITE DIFFERENCE SOLUTION PROCEDURE

3.1 Discretization

Eqns. (15)-(18), constitute a dimensionless nonlinear thermofluid dynamic boundary value problem which does not have a solution with the analytical procedure. However, numerical procedures can provide a solution with high accuracy. In this respect, an implicit finite difference (*Crank-Nicolson type* [47]) procedure is deployed which is *unconditionally stable*. The discretized equations for Eqns. (15) to (17) are obtained as:

$$\frac{U_{f,g}^{h+1}-U_{f-1,g}^{h+1}+U_{f,g}^{h}-U_{f-1,g}^{h}}{2\Delta X}+\frac{V_{f,g}^{h+1}-V_{f,g-1}^{h+1}+V_{f,g}^{h}-V_{f,g-1}^{h}}{2\Delta R}+V_{f,g}^{h+1}(JR)=0$$

(20)

$$\frac{U_{f,g}^{h+1}-U_{f,g}^{h}}{\Delta t}+U_{f,g}^{h}\frac{\left(U_{f,g}^{h+1}-U_{f-1,g}^{h+1}+U_{f,g}^{h}-U_{f-1,g}^{h}\right)}{2\Delta X}+V_{f,g}^{h}\frac{\left(U_{f,g+1}^{h+1}-U_{f,g-1}^{h+1}+U_{f,g+1}^{h}-U_{f,g-1}^{h}\right)}{4\Delta R}$$

$$=AC(Gr)\frac{T_{f,g}^{h}+T_{f,g}^{h+1}}{2}+AB(JR)\frac{\left(U_{f,g+1}^{h+1}-U_{f,g-1}^{h+1}+U_{f,g+1}^{h}-U_{f,g-1}^{h}\right)}{4\Delta R}$$

$$+AB\frac{\left(U_{f,g-1}^{h+1}-2U_{f,g}^{h+1}+U_{f,g+1}^{h+1}+U_{f,g-1}^{h}-2U_{f,g}^{h}+U_{f,g+1}^{h}\right)}{2(\Delta R)^2}+A\alpha_1\left[\frac{\left(U_{f,g-2}^{h+1}-2U_{f,g}^{h+1}+U_{f,g+2}^{h+1}-U_{f,g-2}^{h}+2U_{f,g}^{h}-U_{f,g+2}^{h}\right)}{4(\Delta R)^3(\Delta t)}\right.$$

$$+\frac{\left(U_{f,g+1}^{h+1}-U_{f,g-1}^{h+1}+U_{f,g+1}^{h}-U_{f,g-1}^{h}\right)}{2(\Delta R)(\Delta t)}+V_{f,g}^{h}\frac{\left(U_{f,g+2}^{h+1}-2U_{f,g+1}^{h+1}+2U_{f,g-1}^{h+1}-U_{f,g-2}^{h+1}+U_{f,g+2}^{h}-2U_{f,g+1}^{h}+2U_{f,g-1}^{h}-U_{f,g-2}^{h}\right)}{4(\Delta R)^3}$$

$$+\frac{\left(V_{f,g+1}^{h}-V_{f,g-1}^{h}\right)}{2\Delta R}\frac{\left(U_{f,g-1}^{h+1}-2U_{f,g}^{h+1}+U_{f,g+1}^{h+1}+U_{f,g-1}^{h}-2U_{f,g}^{h}+U_{f,g+1}^{h}\right)}{(\Delta R)^2}$$

$$+3\frac{\left(U_{f,g}^{h}-U_{f-1,g}^{h}\right)}{(\Delta X)}\frac{\left(U_{f,g-1}^{h+1}-2U_{f,g}^{h+1}+U_{f,g+1}^{h+1}+U_{f,g-1}^{h}-2U_{f,g}^{h}+U_{f,g+1}^{h}\right)}{2(\Delta R)^2}+\frac{\left(V_{f,g-1}^{h}-2V_{f,g}^{h}+V_{f,g+1}^{h}\right)}{4(\Delta R)^2}$$

$$\frac{\left(U_{f,g+1}^{h+1}-U_{f,g-1}^{h+1}+U_{f,g+1}^{h}-U_{f,g-1}^{h}\right)}{(\Delta R)}+\frac{\left(U_{f,g+1}^{h}-U_{f,g-1}^{h}\right)}{\Delta R}\frac{\left(U_{f,g+1}^{h+1}-U_{f-1,g-1}^{h+1}+U_{f,g+1}^{h}-U_{f-1,g-1}^{h}\right)}{2(\Delta X)(\Delta R)}+$$

$$(JR)V_{f,g}^{h}\frac{\left(U_{f,g-1}^{h+1}-2U_{f,g}^{h+1}+U_{f,g+1}^{h+1}+U_{f,g-1}^{h}-2U_{f,g}^{h}+U_{f,g+1}^{h}\right)}{2(\Delta R)^{2}}+$$

$$(JR)U_{f,g}^{h}\frac{\left(U_{f,g+1}^{h+1}-U_{f-1,g+1}^{h+1}-U_{f,g-1}^{h+1}+U_{f-1,g-1}^{h+1}+U_{f,g+1}^{h}-U_{f-1,g+1}^{h}-U_{f,g-1}^{h}+U_{f-1,g-1}^{h}\right)}{4(\Delta R)(\Delta X)}+$$

$$3(JR)\frac{\left(U_{f,g}^{h}-U_{f-1,g}^{h}\right)}{(\Delta X)}\frac{\left(U_{f,g+1}^{h+1}-U_{f,g-1}^{h+1}+U_{f,g+1}^{h}-U_{f,g-1}^{h}\right)}{4(\Delta R)}+\frac{3(JR)}{8}\frac{\left(V_{f,g+1}^{h}-V_{f,g-1}^{h}\right)}{\Delta R}\frac{\left(U_{f,g+1}^{h+1}-U_{f,g-1}^{h+1}+U_{f,g+1}^{h}-U_{f,g-1}^{h}\right)}{(\Delta R)^{2}}\Bigg]+$$

$$A\alpha_{2}\Bigg[(JR)\frac{\left(V_{f,g+1}^{h}-V_{f,g-1}^{h}\right)}{\Delta R}\frac{\left(U_{f,g+1}^{h+1}-U_{f,g-1}^{h+1}+U_{f,g+1}^{h}-U_{f,g-1}^{h}\right)}{\Delta R}+(JR)\frac{\left(U_{f,g+1}^{h+1}-U_{f,g-1}^{h+1}+U_{f,g+1}^{h}-U_{f,g-1}^{h}\right)}{2(\Delta R)}$$

$$\frac{\left(U_{f,g}^{h}-U_{f-1,g}^{h}\right)}{(\Delta X)}+\frac{\left(U_{f,g}^{h}-U_{f-1,g}^{h}\right)}{(\Delta X)}\frac{\left(U_{f,g-1}^{h+1}-2U_{f,g}^{h+1}+U_{f,g+1}^{h+1}+U_{f,g-1}^{h}-2U_{f,g}^{h}+U_{f,g+1}^{h}\right)}{(\Delta R)^{2}}+\frac{\left(U_{f,g+1}^{h+1}-U_{f,g-1}^{h+1}+U_{f,g+1}^{h}-U_{f,g-1}^{h}\right)}{2\Delta R}$$

$$\frac{\left(V_{f,g-1}^{h}-2V_{f,g}^{h}+V_{f,g+1}^{h}\right)}{(\Delta R)^{2}}+\frac{\left(U_{f,g+1}^{h}-U_{f,g-1}^{h}\right)}{2(\Delta R)}\frac{\left(U_{f,g+1}^{h+1}-U_{f-1,g-1}^{h+1}+U_{f,g+1}^{h}-U_{f-1,g-1}^{h}\right)}{(\Delta X)(\Delta R)}+\frac{\left(V_{f,g+1}^{h}-V_{f,g-1}^{h}\right)}{2(\Delta R)}$$

$$\frac{\left(U_{f,g-1}^{h+1}-2U_{f,g}^{h+1}+U_{f,g+1}^{h+1}+U_{f,g-1}^{h}-2U_{f,g}^{h}+U_{f,g+1}^{h}\right)}{(\Delta R)^{2}}\Bigg]+A\beta\Bigg[(JR)\frac{\left(U_{f,g+1}^{h}-U_{f,g-1}^{h}\right)^{3}}{4(\Delta R)^{3}}+$$

$$3\frac{\left(U_{f,g+1}^{h}-U_{f,g-1}^{h}\right)^{2}}{4(\Delta R)^{2}}\frac{\left(U_{f,g-1}^{h+1}-2U_{f,g}^{h+1}+U_{f,g+1}^{h+1}+U_{f,g-1}^{h}-2U_{f,g}^{h}+U_{f,g+1}^{h}\right)}{(\Delta R)^{2}}\Bigg]+$$

$$A\beta'\Bigg[\frac{\left(U_{f,g+1}^{h}-U_{f,g-1}^{h}\right)^{2}}{(\Delta R)^{2}}\frac{\left(U_{f-1,g}^{h}-2U_{f,g}^{h}+U_{f+1,g}^{h}\right)}{(\Delta X)^{2}}+\frac{1}{8}\frac{\left(U_{f,g}^{h}-U_{f-1,g}^{h}\right)}{(\Delta X)}\frac{\left(U_{f,g+1}^{h}-U_{f,g-1}^{h}\right)}{(\Delta R)}$$

$$\frac{\left(U_{f,g+1}^{h+1}-U_{f-1,g+1}^{h+1}-U_{f,g-1}^{h+1}+U_{f-1,g-1}^{h+1}+U_{f,g+1}^{h}-U_{f-1,g+1}^{h}-U_{f,g-1}^{h}+U_{f-1,g-1}^{h}\right)}{(\Delta X)(\Delta R)}\Bigg]-AM\left[\frac{U_{f,g}^{h}+U_{f,g}^{h+1}}{2}\right]$$

(21)

$$\frac{T_{f,g}^{h+1}-T_{f,g}^{h}}{\Delta t}+U_{f,g}^{h}\frac{\left(T_{f,g}^{h+1}-T_{f-1,g}^{h+1}+T_{f,g}^{h}-T_{f-1,g}^{h}\right)}{2\Delta X}+V_{f,g}^{h}\frac{\left(T_{f,g+1}^{h+1}-T_{f,g-1}^{h+1}+T_{f,g+1}^{h}-T_{f,g-1}^{h}\right)}{4\Delta R}$$

$$=\frac{D}{Pr}\left(E+\frac{4}{3Nr}\right)\Bigg[\frac{\left(T_{f,g-1}^{h+1}-2T_{f,g}^{h+1}+T_{f,g+1}^{h+1}+T_{f,g-1}^{h}-2T_{f,g}^{h}+T_{f,g+1}^{h}\right)}{2(\Delta R)^{2}}+(JR)\frac{\left(T_{f,g+1}^{h+1}-T_{f,g-1}^{h+1}+T_{f,g+1}^{h}-T_{f,g-1}^{h}\right)}{4(\Delta R)}\Bigg]$$

(22)

The considered flow domain is defined by the limits (boundaries): $X_{min} = 0,\ X_{max} = 1, R_{min} = 1$ and $R_{max} = 20$ (where R_{max} implies to $R = \infty$). The temperature Eqn. (22) and momentum Eqn. (21) equations are discretized for all internal mesh points (f, g) at specific 'f - level' can be reduced to 'tridiagonal' and 'penta-diagonal' system of equations which are respectively represented as:

$$A_1\delta_{f,g-1}^{h+1} + B_1\delta_{f,g}^{h+1} + C_1\delta_{f,g+1}^{h+1} = D_1 \tag{23}$$

$$A_2\gamma_{f,g-2}^{h+1} + B_2\gamma_{f,g-1}^{h+1} + C_2\gamma_{f,g}^{h+1} + D_2\gamma_{f,g+1}^{h+1} + E_2\gamma_{f,g+2}^{h+1} = F_2 \tag{24}$$

At $(h+1)^{th}$ level, 'tridiagonal' [47] and 'penta-diagonal' [48] algorithms are used to solve the system of Eqns. (23) and (24). Here, δ & γ represent T & U, respectively. Details on these algorithms can be found in [23], [24]. The computational procedure commences initially to find a solution for the temperature field (solving Eqn. (22) for T) and thereafter the numerical code solves for the velocity field i. e. Eqn. (21) for U. The generated U, T values are used explicitly to calculate V from Eqn. (20).

3.2 Validation test of the Crank-Nicolson numerical scheme

Validation of the implemented numerical scheme (Crank-Nicolson finite difference method) is carried out in two-step process. In the first stage of validation, mesh independence ensures the accuracy of the scheme. In the second stage, the simulated results are validated with previous literature.

3.2-1 Mesh Independence

The proposed grid system for the current study is optimized by a '*grid-independency test*' and thereby mesh density can be selected to be computationally accurate but also economically desirable. **Table 3** documents the optimal grid-size (i.e., 100 X 500) which attains sufficient accuracy (any other refinement in the mesh-size does not support an improvement in the accuracy).

Correspondingly, '*time-independency test*' offers the finest time-step size Δt $(t = h\Delta t, h = 0, 1, 2, \ldots) = 0.01$ as provided in **Table 4**.

3.2-2 Comparison with former special cases from the literature

The transient plots of numerical solutions for $\overline{C_f}$ and $\overline{Nu}$ provide a good basis for benchmarking with previous simpler models from the literature. The case of fluid flow past a cylinder ($\gamma = 0$) allows a comparison with previously published results, to verify the preciseness of the Crank Nicolson computational code. Therefore, in the present model, nanoscale effects (such as volume fraction, φ) and viscoelastic behaviour of third-grade fluid (α_1, α_2, β) are ignored, and furthermore, the magnetic field is neglected (M = 0 i.e. electrically non-conducting scenario) and thermal radiation negated (Nr = 0) so that the general model developed in this article is reduced to *Newtonian* flow (i.e., $\alpha_1 = \alpha_2 = \beta = \beta' = 0$) and then matches exactly the model reported in Rani and Kim [49] ($\gamma = 0$). **Fig. 2 (**comparison graph) confirms the accuracy of the Crank-Nicolson code which achieves a very close correlation with the results in [49].

4. GRAPHICAL RESULTS AND DISCUSSION

The velocity and temperature graphs of the third-grade nanofluids under steady and unsteady conditions are visualized in **Figs. 3-15** for the impact of key thermophysical, hydrodynamic and nanoscale parameters such as volume fraction (φ), third-grade fluid parameter (β), Prandtl number (Pr), Grashof number (Gr) and radiative parameter (N). Steady-state graphs of (U & T) for variation of β & φ over a moving ($\gamma = 1$) and stationary ($\gamma = 0$) cylinder are drawn. Transient results of skin friction and heat transfer rate for variation of third-grade parameter and volume fraction are additionally depicted through graphs. Present work includes four types of nanofluids containing nanoparticles (TiO_2, Cu, and Al_2O_3) with non-Newtonian third-grade fluid as base fluid. Throughout the study $\alpha_1 = \alpha_2 = 0.001$ and modified third-grade parameter $\beta' = 0.001$. Effect on rate of heat transfer by changing the shape of the nanoparticles is also plotted. The considered range of volume fraction of nanoparticle is $0 \leq \varphi \leq 0.04$, since sedimentation of

nanoparticle takes place when $\varphi > 8\%$. In the current problem, the shape of the nanoparticles is spherical with thermal conductivity and dynamic viscosity (refer to model **(i)** in **Table 2**). On these details, the following subsections provide a comprehensive discussion.

Comparative results Al_2O_3-SA nanofluid for stationary and moving cylinder

The computed numeric values reflect the relative heat transfer due to the convective flow of third-grade nanofluid (Al_2O_3-*SA*) over moving and stationary cylinders. Here, the movement of the cylinder is signified by the boundary condition referred to in Eq. (18) i.e., $\gamma = 0$ or 1. **Table 5** presents that heat transfer significantly increases from stationary ($\gamma = 0$) to moving ($\gamma = 1$) cylinder. Also, the following discussion clearly represents the results on the velocity of the flow and temperature of the flow regime for both cases (i.e., $\gamma = 0$ &1).

Table 1. Thermophysical conditions of the nanoparticles and base fluid (Mahanthesh et al. (2016) and Rajesh et al. (2017)).

	$\rho(kgm^{-3})$	$k(Wm^{-1}k^{-1})$	$C_p(kg^{-1}k^{-1})$	$\beta \times 10^{-5}(k^{-1})$
$C_6H_9NaO_7$ *(SA)*	989	4175	0.613	0.99
Al_2O_3	3970	765	40	0.85
TiO_2	4250	686.2	8.9528	0.90
Cu	8933	385	401	1.67

Table 2. Dynamic viscosity and thermal conductivity for different shapes of nanoparticles (Rajesh et al. (2017)).

Model	Shape of nanoparticles	Dynamic viscosity	Thermal conductivity
(i)	Spherical	$\mu_{nf} = \frac{\mu_{bf}}{(1-\varphi)^{2.5}}$	$\frac{k_{nf}}{k_{bf}} = \frac{k_s + 2k_{bf} - 2\varphi(k_{bf} - k_s)}{k_s + 2k_{bf} + \varphi(k_{bf} - k_s)}$
(ii)	Spherical	$\mu_{nf} = \mu_{bf}(1 + 7.3\varphi + 123\varphi^2)$	$\frac{k_{nf}}{k_{bf}} = \frac{k_s + 2k_{bf} - 2\varphi(k_{bf} - k_s)}{k_s + 2k_{bf} + \varphi(k_{bf} - k_s)}$

(iii)	Cylindrical	$\mu_{nf} = \frac{\mu_{bf}}{(1-\varphi)^{2.5}}$	$\frac{k_{nf}}{k_{bf}} = \frac{2k_s + k_{bf} - 2\varphi(k_{bf} - k_s)}{2k_s + k_{bf} + 2\varphi(k_{bf} - k_s)}$
(iv)	Cylindrical	$\mu_{nf} = \mu_{bf}(1 + 7.3\varphi + 123\varphi^2)$	$\frac{k_{nf}}{k_{bf}} = \frac{2k_s + k_{bf} - 2\varphi(k_{bf} - k_s)}{2k_s + k_{bf} + 2\varphi(k_{bf} - k_s)}$

Table 3. Grid independency test.

Grid size	**Average Nusselt number** $\boldsymbol{\alpha_1 = \alpha_2 = \beta' = 0.001, \beta = 0.06, \varphi = 0.04, Pr = 6.2, Gr = 10, M = 0.001, N = 0.01}$
25X125	0.5165231000
50X250	0.5199731000
100X500	0.5288731000
200X1000	0.5211731000

Table 4. Time independency test.

Time step size $\boldsymbol{(\Delta t)}$	**Average Nusselt number** $\boldsymbol{\alpha_1 = \alpha_2 = \beta' = 0.001, \beta = 0.06, \varphi = 0.04, Pr = 6.2, Gr = 10, M = 0.001, N = 0.01}$
0.1	0.5288700000
0.08	0.5288700000
0.05	0.5288705000
0.02	0.5288727000
0.01	0.5288731000

Table 5. Comparing heat transfer coefficient between stationary and moving cylinders for different values of β and φ.

Third-grade fluid parameter $\boldsymbol{(\beta)}$	**Volume fraction parameter** $\boldsymbol{(\varphi)}$	**Heat transfer coefficient measured at stationary cylinder** $\boldsymbol{(\gamma = 0)}$ $\boldsymbol{(\overline{Nu})}$	**Heat transfer coefficient measured at moving cylinder** $\boldsymbol{(\gamma = 1)}$ $\boldsymbol{(\overline{Nu})}$
0.02	0.02	0.5210	0.5621
0.02	0.03	0.5364	0.5789
0.02	0.04	0.5522	0.5960
0.04	0.04	0.5381	0.5844
0.06	0.04	0.5288	0.5767

Table 6. Effects of Prandtl number (Pr), Grashof number (Gr) & radiative parameter (N) on heat transfer coefficient for the stationary cylinder.

Prandtl number *(Pr)*	**Radiative parameter** *(Nr)*	**Grashof number** *(Gr)*	**Temporal maximum (t) of T**	**Steady-state time t**	**Maximum temperature (T) at $X = 1$**	**Heat transfer coefficient measured at stationary cylinder ($\gamma = 0$) ($\overline{Nu}$)**
6.2	0.01	10	0.63	5.36	0.9460	0.5522
13.4	0.01	10	0.73	3.89	0.9301	0.7128
13.4	0.02	10	0.85	5.56	0.9131	0.8818
13.4	0.02	05	1.08	5.85	0.9238	0.7681

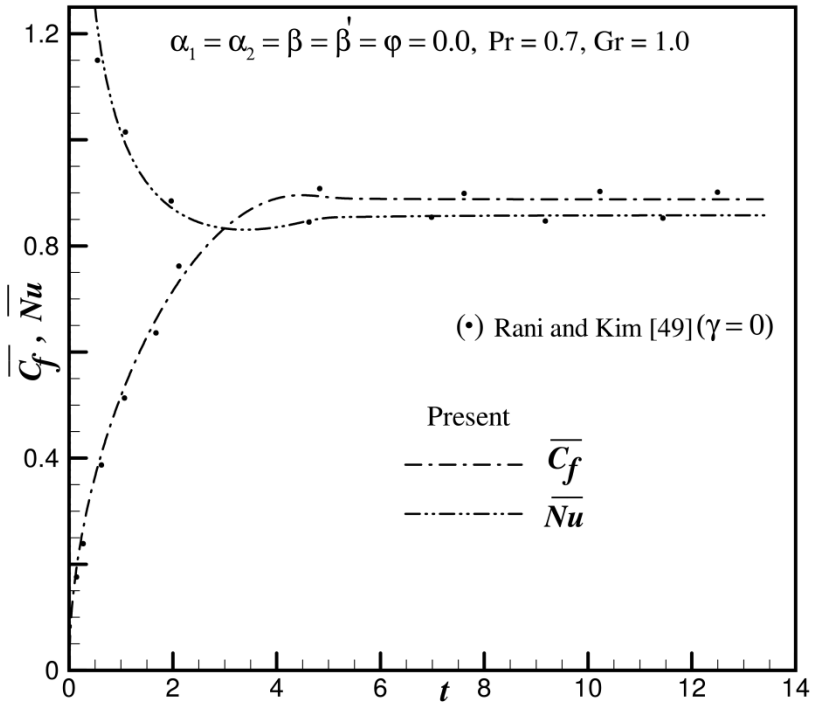

Fig. 2 Comparison result for a Newtonian fluid

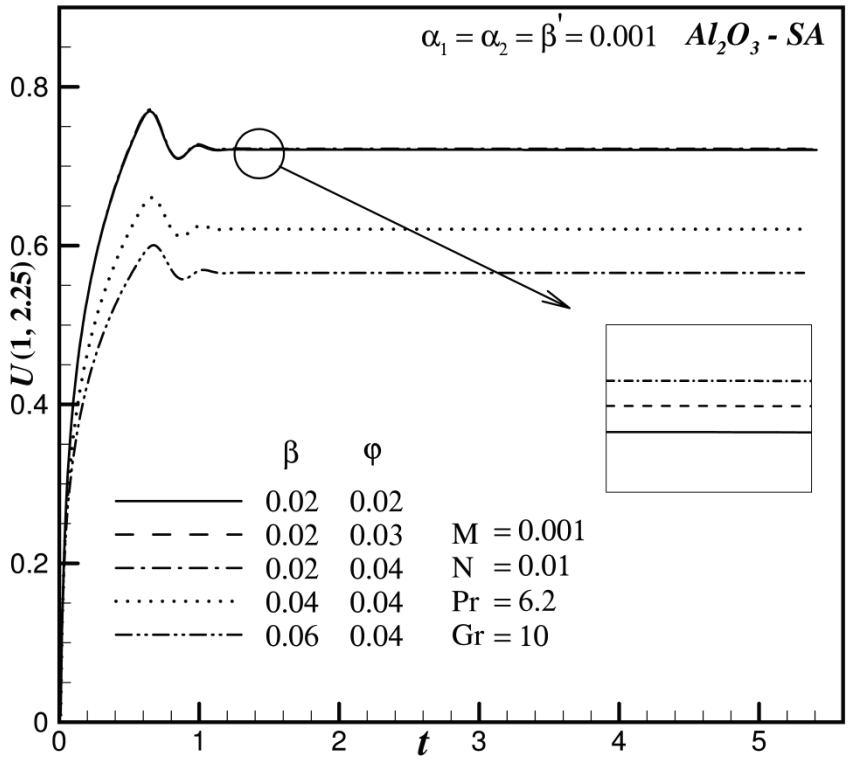

Fig. 3 Transient non-dimensional velocity profile for variation of third-grade fluid parameter and volume fraction.

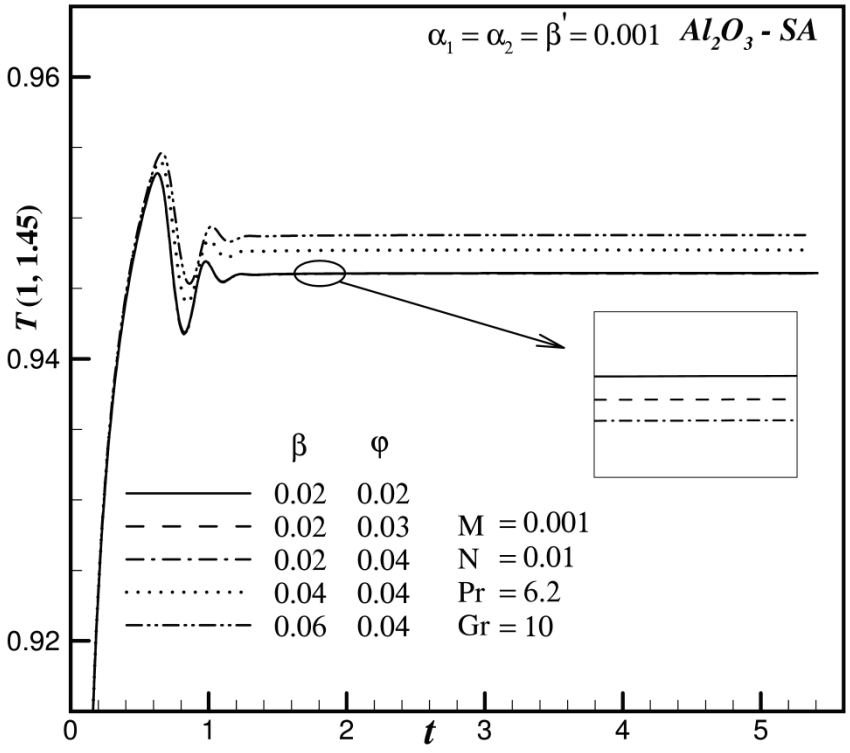

Fig. 4 Transient non-dimensional temperature profile for variation of third-grade fluid parameter and volume fraction.

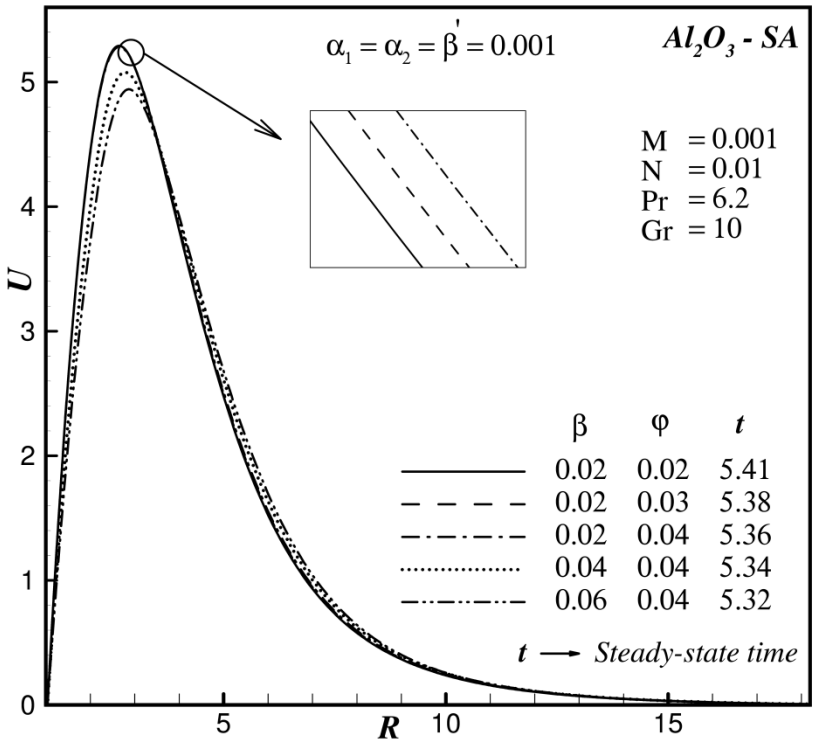

Fig. 5 Steady dimensionless velocity profile for variation of third-grade fluid parameter and volume fraction.

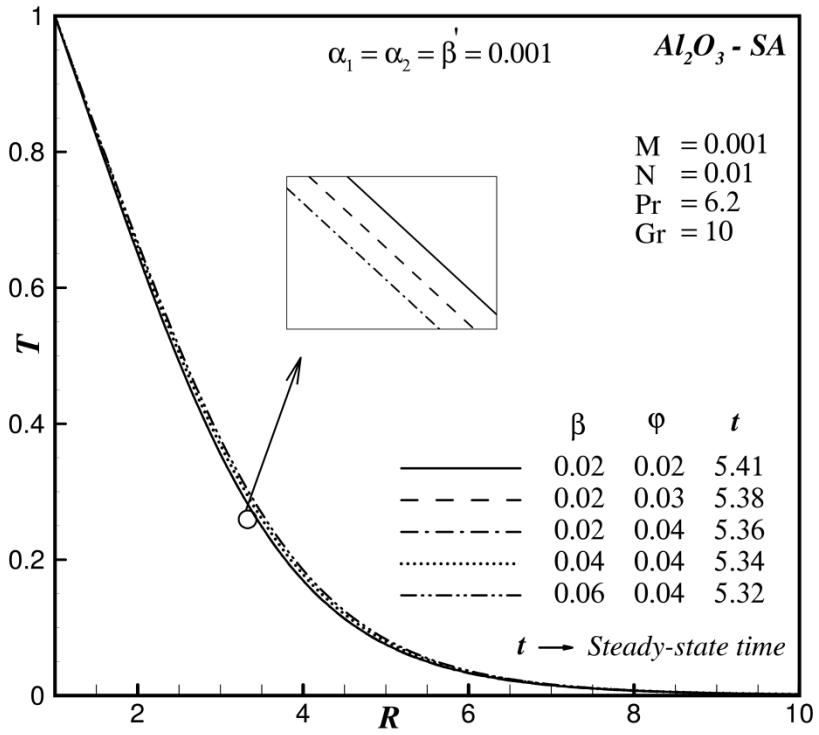

Fig. 6 Steady-state dimensionless temperature profile for variation of third-grade fluid parameter and volume fraction.

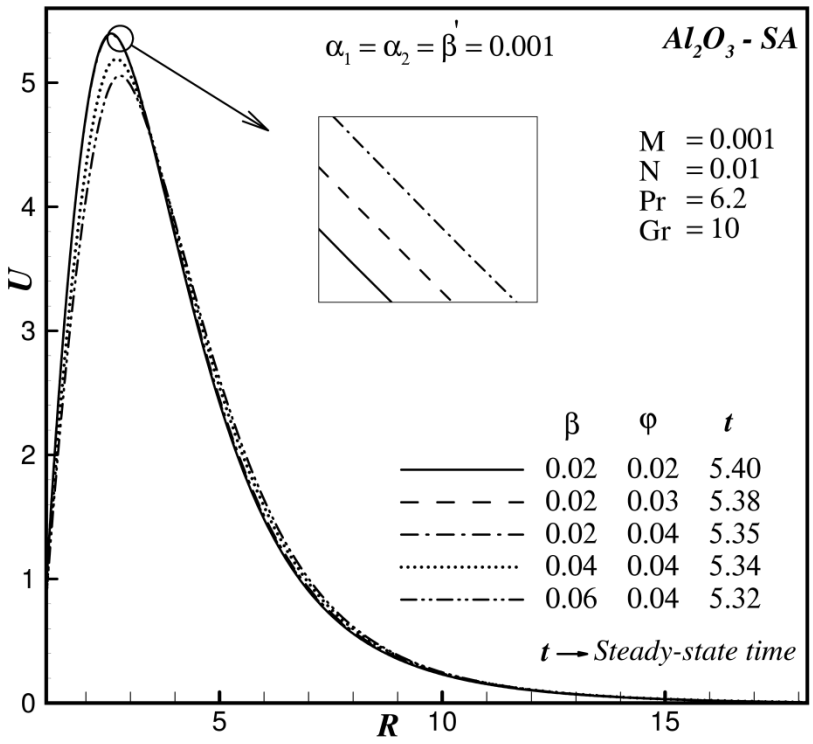

Fig. 7 Steady-state dimensionless velocity profile for variation of third-grade fluid parameter and volume fraction: moving cylinder.

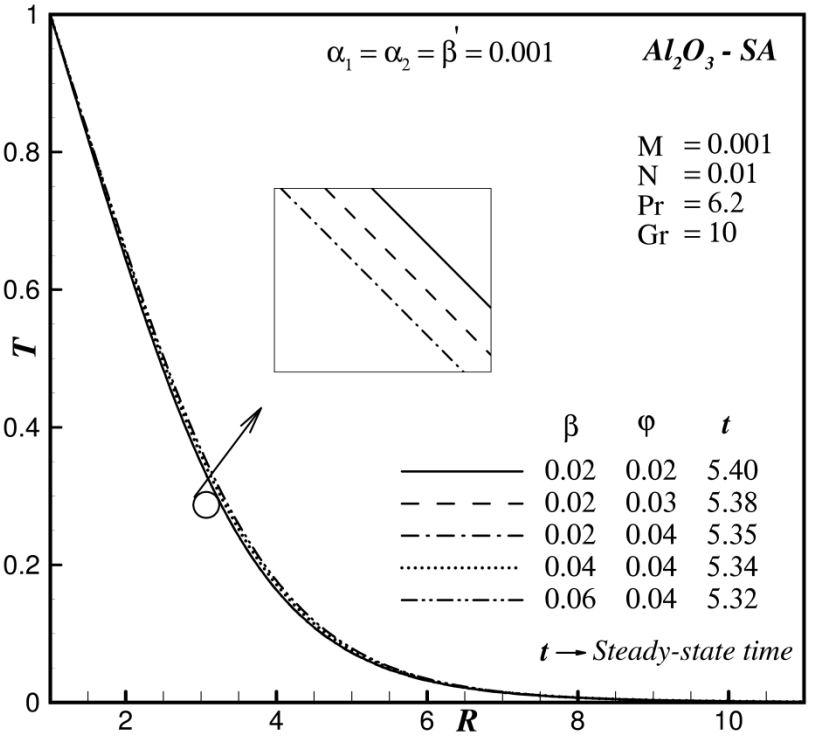

Fig. 8 Steady-state dimensionless temperature profile for variation of third-grade fluid parameter and volume fraction: moving cylinder.

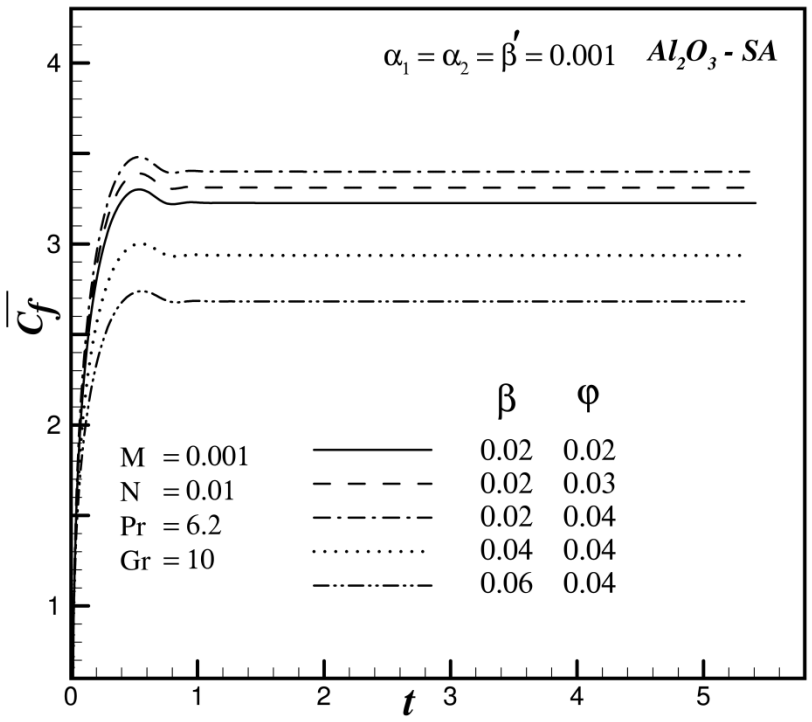

Fig. 9 Skin friction values for different values of third-grade fluid parameter and volume fraction.

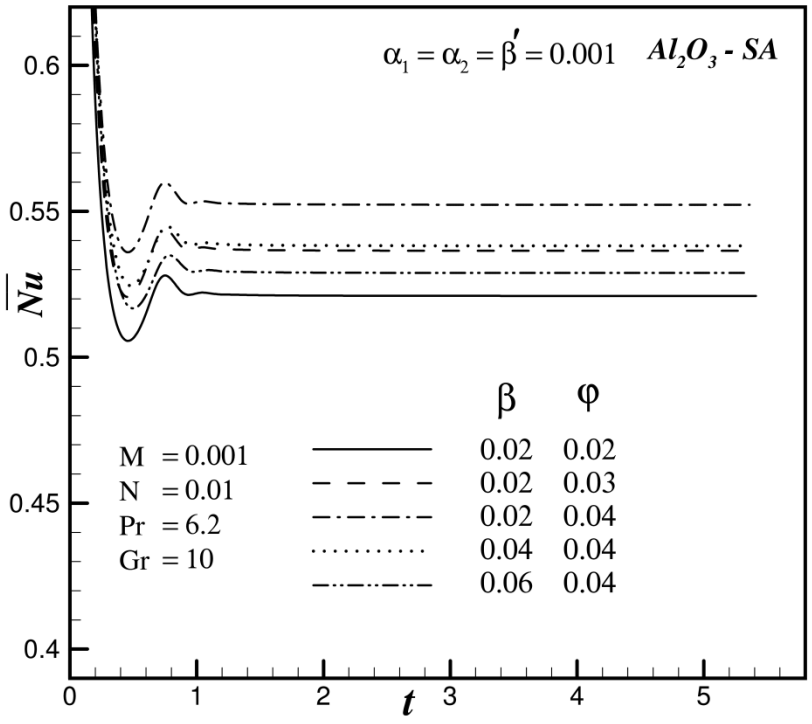

Fig. 10 Nusselt number values for different values of third-grade fluid parameter and volume fraction.

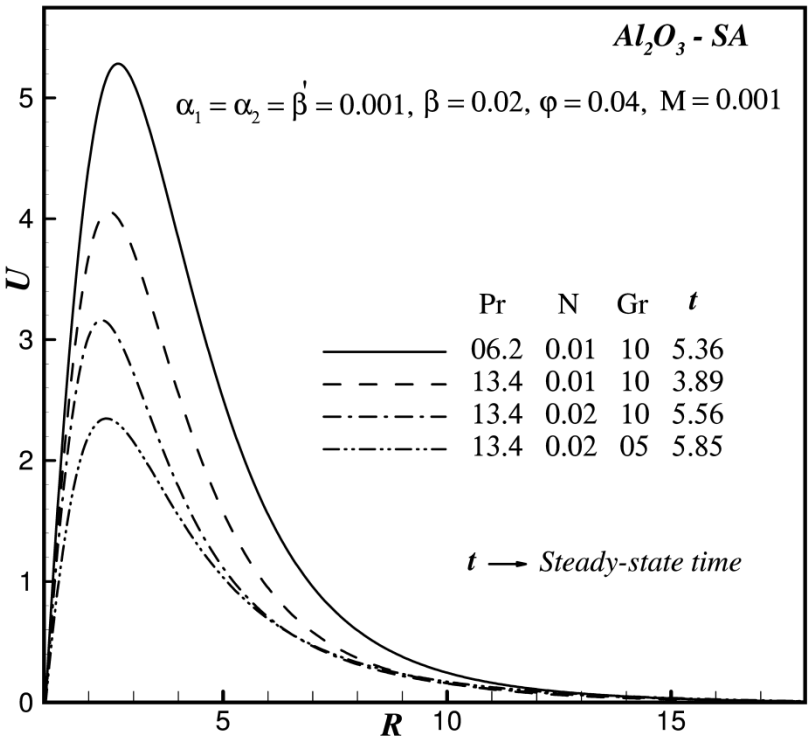

Fig. 11 Steady-state dimensionless velocity plot for different parameter; (a) Prandtl number, (b) radiative parameter & (c) Grashof number.

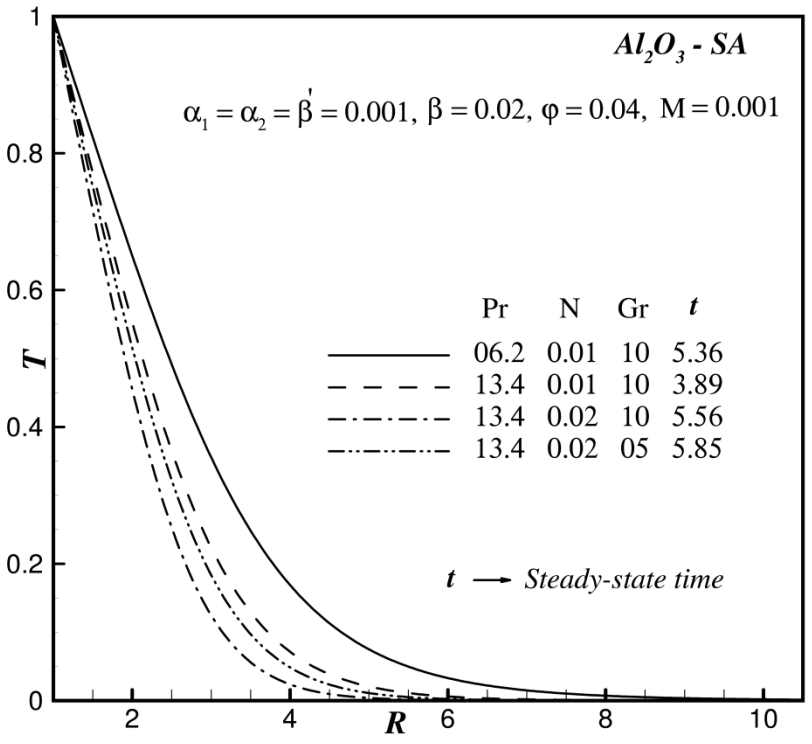

Fig. 12 Steady-state dimensionless temperature plot for different parameter; (a) Prandtl number, (b) radiative parameter & (c) Grashof number.

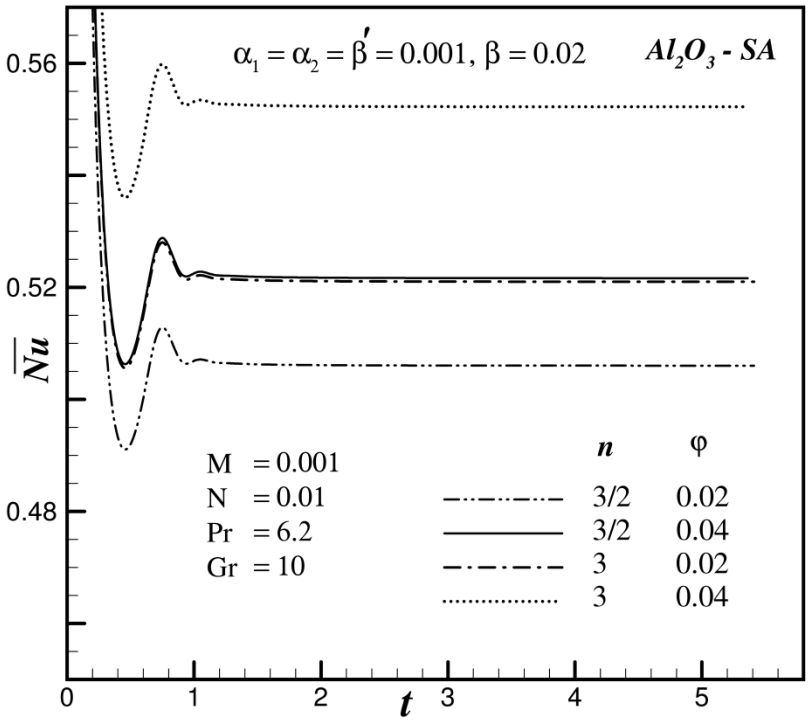

Fig. 13 Effect of shape of nanoparticles on the rate of heat transfer with variation in volume fraction values.

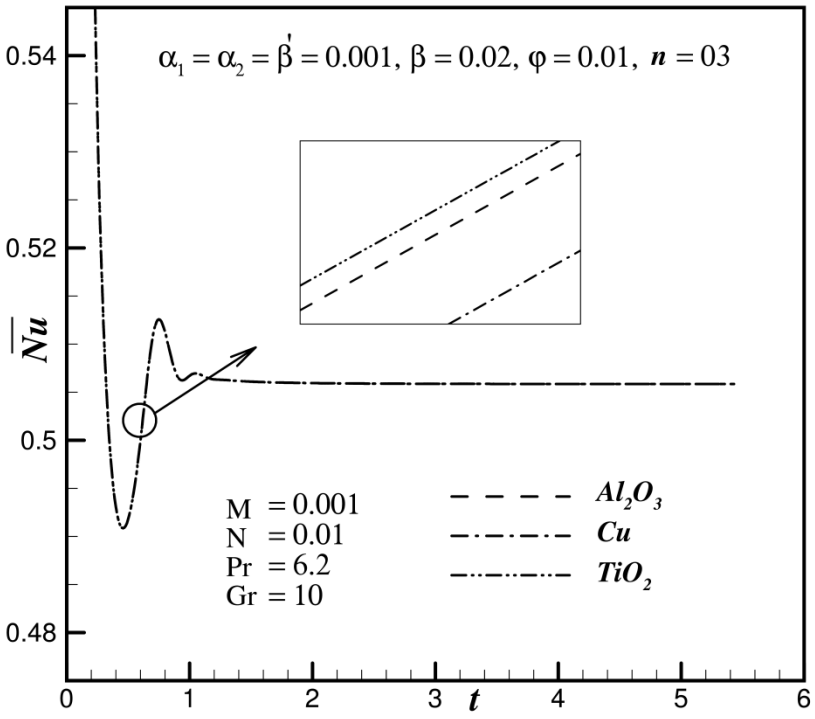

Fig. 14 Rate of heat transfer for various nanofluids.

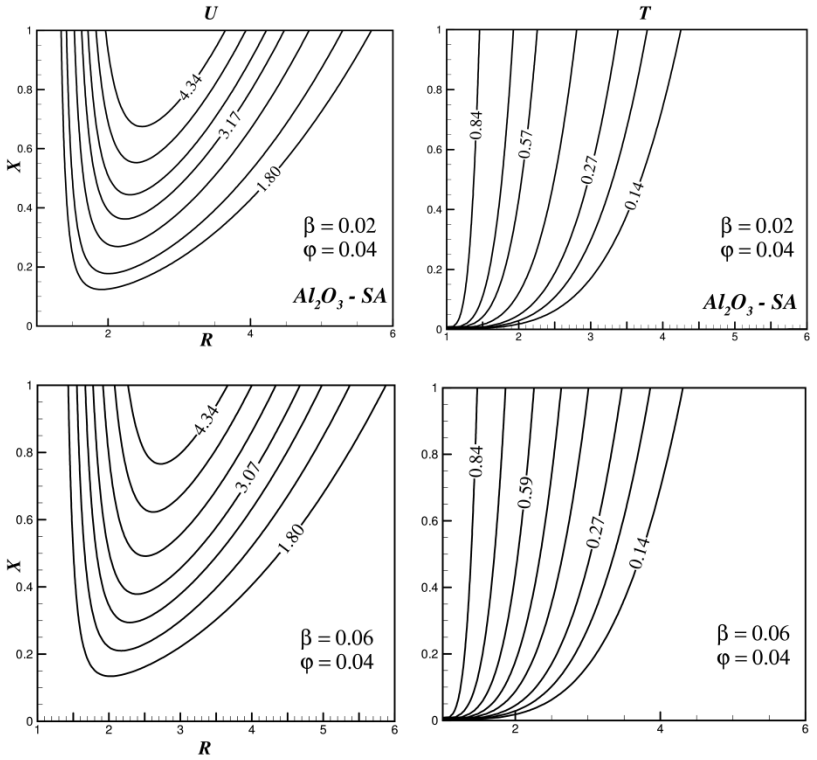

(a)

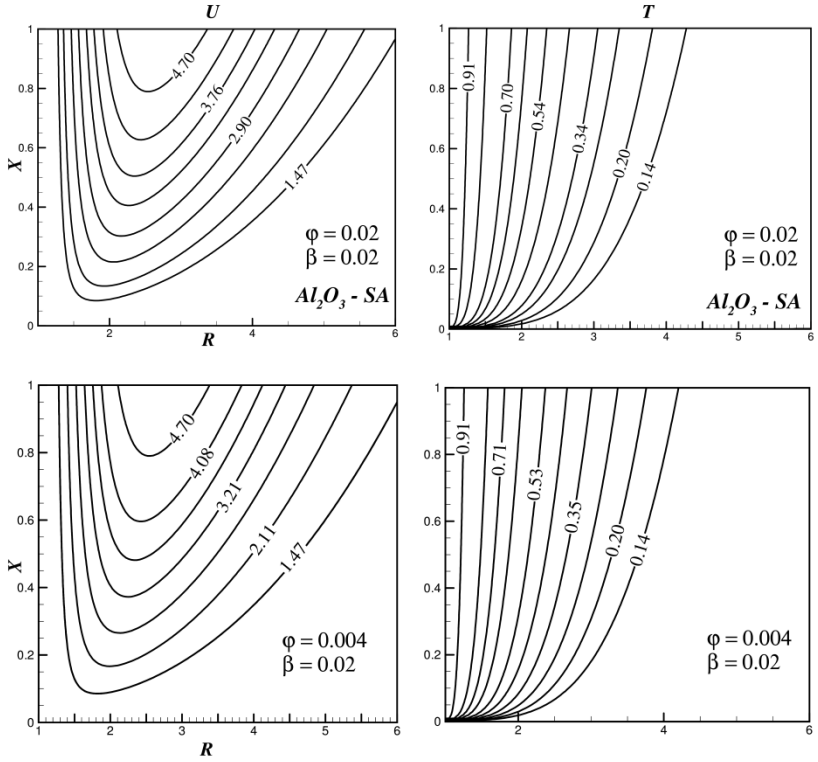

(b)

Fig. 15 Steady-state contour plots of velocity (*U*), temperature (*T)* for variation of (a) third-grade fluid parameter; (b) volume fraction, keeping all other parameters fixed.

(i)Transient profiles of the stationary cylinder $(\gamma = 0)$*;*

The numerically simulated transient velocity (*U*) profile of *Al_2O_3-SA* third-grade nanofluid for variation of third-grade fluid parameter (β) and volume fraction (φ) (keeping other parameters constant) at a specific location (1, 2.25) is depicted in **Fig. 3**. The *U* curves maintain a particular trend i.e., initial growth is observed in the curves which then reach a peak value, and eventually a time-independent state is attained. Also, $t << 1$ is the time where the *conductive* mode of heat transfer dominates over the *convective* mode. At later stages in time, the contrary behaviour is present i. e. convection heat transfer dominates conduction heat transfer. From **Fig. 3**, the *U* curves of *Al_2O_3-SA* third-grade nanofluid at $\varphi = 0.04$ show a decreasing trend with amplifying values of β. Significant deceleration is induced in the viscoelastic nanofluid boundary layer coating flow with a stronger rheological effect since viscosity is increased and momentum diffusion rate is reduced. Hydrodynamic boundary layer thickness will therefore be increased on the cylinder periphery. Similarly, *U* profile of *Al_2O_3-SA* at constant $\beta = 0.02$, increases with increasing volume fraction (φ). In other words, the enhanced doping of the nanoliquid modifies the viscosity and accelerates the flow resulting in a thinner hydrodynamic (velocity) boundary layer thickness on the cylinder surface. In both cases i.e., with increasing φ or β values, the time taken to attain the steady-state increases. It can also be observed that magnitude of a peak value of the velocity of *Al_2O_3-SA* nanofluid increases for amplifying values of φ (or β) at constant β (or φ).

Transient non-dimensional temperature (*T*) curves of *Al_2O_3-SA* third-grade nanofluid for variation of β (third-grade fluid parameter) and of φ (volume fraction) at the coordinates (1, 1.45) are shown graphically in **Fig. 4**. Here, $Pr = 6.2$, $GR = 10$, $N = 0.01$ & $M = 0.001$. Initially, these profiles are elevated with time and thereafter become independent of time. Temperature is therefore boosted with progression in time and thermal boundary layer thickness is enhanced on the cylinder surface. Temperature curves show a similar transient behavior at any location in the flow-domain. It is also apparent that with increment in viscoelastic parameter, β, T

curves overlap with each other at the initial stages in time. A similar response is observed with variation in φ value. This overlapping nature of the curves is due to the heat conduction effect which is most prominent at the initial time. After reaching the temporal peak, temperature distributions clearly deviate from each other and show significant variation with modification in β or φ. The third-grade fluid parameter i.e., β defines the effect of viscoelasticity in boundary layer flow (i.e. relative effect of elastic & viscous forces). As β augments, the viscosity nature stimulates & the elastic behavior of the fluid decreases which slowdowns the flow. A decreased velocity of the fluid is presented clearly in Fig. 3. Correspondingly, because of greater viscosity & lesser elastic properties, the collisions between the fluid particles (*greater momentum diffusion*) enhance hence resulting in heating of the boundary layer. The magnitude of temperature value therefore noticeably amplifies for higher β value at $\varphi = 0.04$, and thermal boundary layer thickness is maximized for this scenario. Furthermore the T profile for $\beta = 0.02$ increases as φ enhances. Higher φ value increases the number of nanoparticles in the flow-field hence there will be more heat transfer.

(ii)Steady-state profiles of the stationary cylinder $(\gamma = 0)$*;*

Steady-state velocity (U) curves of Al_2O_3-*SA* third-grade nanofluid at constant Pr, Gr, N & M with variations in β and φ are represented in **Fig. 5**. In this case, the cylinder is stagnant. The U curves for non-Newtonian nanofluid (Al_2O_3-*SA*) follow the same topology for variation of both parameters (φ and β). In both cases (i.e., increasing β or φ), U i. e. velocity magnitude increases (flow acceleration is induced), eventually attaining a maximum value, and then gradually decreases to $U = 0$. Here, reaching the peak value (U_{max}) needs more time with lower values of viscoelastic parameter β or volume fraction φ. The U profiles in the region $0 < R < 3.5$, exhibit a decreasing trend whereas for the region after $R = 3.5$, they show an increasing trend with increasing β. The viscoelasticity, therefore, has a complex interplay with momentum diffusion in the boundary layer and this is dependent on location.

At coordinates (1, 1.15), the dimensionless temperature (T) evolution with the radial coordinate, R for *Al_2O_3-SA* nanofluid and variation in β and φ (with maintained values of Pr, Gr, N & M) is displayed in **Fig. 6**. Since the temperature is also a function of time, T curves initially take the value $T = 1$ (i.e., *boundary condition preserved at the hot surface of a cylinder*) and with progress in time, the magnitudes are reduced, plummeting finally to the lowest value (i.e., $T = 0$ in the free stream). Also, heat transfer by conductive mode can be observed at the starting time. As β amplifies, the thermal boundary layer thickness is boosted; however, the opposite effect is induced in the T profile with increasing values of φ. It is also noteworthy that the temperature, T, curve attains the steady-state stage earlier with increment in β or φ.

(iii) Steady-state profiles of moving cylinder ($\gamma = 1$)*;*

Figure 7 displays the time-independent plot of velocity for third-grade nanofluid (*Al_2O_3-SA*) versus R (radial direction) for different values of φ and β where Pr, Gr, N & M are maintained at a constant value. Here, the considered curved geometry ('cylinder') is impulsively moving ($\gamma = 1$) with velocity u_0. As such the velocity of natural convective flow of nanofluid is witnessed and it starts from $U = 1$ to attain the U_{max} then drops to $U = 0$. The pattern is the same with either variation in φ or β. The greater β (or φ) is, the thicker the momentum (hydrodynamic) boundary layer will be at the surface of the hot cylinder. The results are more distinctly visible by varying β than φ. Here again, the time taken to achieve the steady-state time is reduced with increasing β or φ, indicating that both viscoelasticity and nanoparticle volume fraction exert a tangible effect on the *transient* behaviour of the velocity in addition to spatially dependent behaviour.

Likewise, the steady-state graph for temperature variation in the radial direction for the moving cylinder is drawn with varying values of third-grade parameter β or volume fraction φ, keeping other parameters as constant (refer to **Fig. 8**). Whether the hot cylinder is *stationary or moving* with velocity u_0, the observations are almost similar i.e., as φ magnifies, the thermal boundary

layer thickness is diminished. Also, for higher β, the thermal boundary layer thickness is elevated and more efficient transport of heat in the bulk fluid is achieved.

Results on coefficients of heat transfer and skin friction

Many industrial applications of nano polymers, material processing, and coating dynamics demand the calculation of $\overline{Nu}$ (heat transfer coefficient) and $\overline{C_f}$ (skin friction) – these quantities are therefore also evaluated here for third-grade nanofluid (*Al_2O_3-SA*) which helps in designing coating thicknesses and sustaining the quality of the finished product. The dimensionless quantities to calculate i.e. $\overline{C_f}$ and $\overline{Nu}$ are given through the following equations.

$$\overline{C_f} = \frac{B}{Re}\int_0^1 \left(\frac{\partial U}{\partial R}\right)_{R=1} dX \tag{25}$$

$$\overline{Nu} = -E\int_0^1 \left(\frac{\partial T}{\partial R}\right)_{R=1} dX \tag{26}$$

where, $Re = \frac{u_0 r_0}{v_f}$ is local (radial) characteristic Reynolds number.

The influence of third-grade fluid parameter (β) and the volume fraction (φ) on the coefficient of skin friction is plotted through **Fig. 9** for constant values of Pr, Gr, N & M. All $\overline{C_f}$ curves increase to a maximum value slightly, descend to a lower value then with progress in time take constant values. As β is raised, $\overline{C_f}$ drops to lower values i.e., retardation is produced in the third-grade nanofluid (*Al_2O_3-SA*) which is also corroborated with the computations shown in **Fig. 3**. This interesting observation is due to the fact that as β enhances the viscoelastic property of third-grade nanofluid intensifies i. e. elastic forces interact differently with viscous force. The momentum diffusion is inhibited and skin friction i. e. the shear stress at the cylinder surface is reduced**. Figure 9** also shows results for varying φ i.e., with augmented values of φ, surface skin friction ($\overline{C_f}$) increases which can be confirmed from **Fig. 3**. Volume fraction (φ) evaluates the number of nanoparticles in the base fluid (third-grade fluid i.e., Sodium Alginate). Here, a higher value of φ means more nanoparticles (Al_2O_3) which result in a high frictional value ($\overline{C_f}$) due to a strong

reduction in the global viscosity of the nanofluid which is exacerbated with intensified collisions between the nanoparticles.

Figure 10 reflects the results for wall heat transfer rate ($\overline{Nu}$) at $R = 1$ (heated surface of a cylinder) for different values of φ & β (Pr, Gr, N & M are constants). At starting time, the $\overline{Nu}$ profile drops drastically to smaller values, amplifies thereafter a time-independent state ensues. For an increasing value of β (third-grade fluid parameter), $\overline{Nu}$ also being a function of time, is observed to decrease. This result is significant since for greater values of β, it has earlier been established that higher temperature values are noticed i. e. heating arises in the boundary layer flow with stronger viscoelasticity which manifests in a thicker thermal boundary layer and more efficient transfer of heat from the cylinder surface (refer **Fig. 4** and Eq. 26). Increasing β value means stronger bond formation between the third-grade nanofluid particles i. e. a tighter matrix structure which enhances the viscoelastic effect. This raises the temperature of the nanofluid (Al_2O_3-*SA*) regime which is reflected in **Fig. 10**. Hence, it heats up the boundary layer regime which implies a reduction in $\overline{Nu}$ value (i.e., rate of heat transfer to wall of the cylinder). For augmenting values of φ (volume fraction), the more number of nanoparticles are added to the flow-field, hence $\overline{Nu}$ increases due to greater heat transfer. **Figure 4** also is consistent with this result.

***Effects of Prandtl number* (Pr), *Grashof number* (Gr) *and radiative parameter* (N)**

For variation in third-grade fluid parameter and volume fraction values, with the constant transverse magnetic field (M_0), $\overline{Nu}$ as a function of time at the wall of the stationary cylinder ($\gamma = 0$) is presented through **Figs. 11 & 12**. In these plots, the influence is shown for Pr, Gr & N effects. Amplified Pr or N value reduces the peak velocity of the nanofluid flow. However, U_{max} increases with greater Gr. The thickness of the thermal boundary layer diminishes for intensified Pr or N value. A qualitatively similar response is computed via augmenting Gr. Increasing Grashof number corresponds to elevation in thermal buoyancy force relative to viscous hydrodynamic force. This exacerbates thermal convection currents which accelerate the flow but deplete the

temperature, a classical result in convection flows. A decrease in temperature value is observed as the Prandtl number relates the momentum and thermal diffusivity. Hence, it has control over the relative thickness of momentum and thermal boundary layers. Also, a similar observation is noticed for greater N values, since the rate of energy transport to the flow-field decreases with the radiation effect. In this regard, **Table 5** shows that, as any of the parameters Pr, Gr or N intensifies, then $\overline{Nu}$ (*heat transfer rate to the surface cylinder*) enhances since temperatures are reduced in the bulk fluid, as established earlier. From **Table 6,** it is verified that T_{max} decreases and $\overline{Nu}$ (based on Eqn. (26)) increases for growing values of Pr, Gr & N. The time for achieving steady-state reduces for higher Pr (or Gr) and lower N.

Shape of the nanoparticle

Figure 13 depicts the rate of heat transfer at $R = 1$ (on the surface of the cylinder) for the radiative convective flow of third-grade nanofluid by changing the shape of nanoparticles (Al_2O_3) and varying volume fraction of the nanofluid. The shape of nanoparticles shows a considerable impact on heat transfer characteristics. In this study, spherical and cylindrical shaped nanoparticles are considered. Heat transfer of flow of third-grade fluid based nanofluid significantly changes by varying n (i.e., the shape of nanoparticle). It is abundantly clear that Nusselt number ($\overline{Nu}$) is greater for *spherical* shaped nanoparticles of Al_2O_3 than cylindrical shaped ones for any particular volume fraction. In mathematics, the sphere is known to possess the unique property of having a maximum volume for the minimum surface area. This enables more nanoparticles to be doped into the regime compared with cylindrical geometries and produces a greater overall surface area for micro-convection between the nanoparticles and the engulfing base fluid. As a result, the effective thermal conductivity k_{nf} is boosted and this produces exceptional elevations in increased $\overline{Nu}$. These observations have been confirmed in many laboratory experiments and indeed in the larger-scale deployment of metallic nanofluids in the coating and other industries. Also, in both cases of n, $\overline{Nu}$ augments for the amplified value of φ. Overall, it may be deduced therefore that *both*

nanoparticle shape and doping percentage (volume fraction) impart *thermal enhancement properties* to base fluids.

Different types of nanoparticle

Figure 14 displays the computational results on heat transfer ($\overline{Nu}$ at $R = 1$) on the wall of the heated curved geometry (cylinder) for third-grade fluid (Sodium Alginate)-based nanofluid for different nanoparticle types (nanomaterials). The current study considers Alumina (Al_2O_3), Copper (*Cu*), and Titanium oxide (TiO_2) as metallic/metallic oxide nanoparticles for natural convective heat transfer coating flow. All other parameters ($Pr, Gr, N,\ M\ \&\ \varphi$) are kept constant. Hear, all $\overline{Nu}$ curves follow the same pattern. It is noticed that by changing the nanoparticles in the base fluid the gap between the $\overline{Nu}$ curves is not significant; however, it is clearly observed that third-grade fluid (*SA*) based nanofluid with Titanium oxide (TiO_2) achieves the highest $\overline{Nu}$ value i.e., the maximum computed rate of heat transfer to the solid surface of cylinder compared with other nanoparticles. The nanofluid with *Cu* nanoparticles has a lesser heat transfer rate than others, even though copper possesses a higher thermal conductivity which will produce higher temperatures within the bulk fluid but lower heat diffusion to the wall, and this is probably also attributable to the base fluid contribution. It is known that Nusselt number is the ratio of convective to conductive heat transfer i.e., as *Cu* exhibits the highest thermal conductivity, Sodium Alginate with *Cu* nanoparticles has the lowest $\overline{Nu}$ value. Copper will therefore energize the bulk fluid most (highest temperatures) and produce a thicker thermal boundary layer but will perform least best in terms of transferring heat to the cylinder surface from the bulk fluid (boundary layer regime).

Contour plots

The rectangular 2D *X-R* plane represents the contour lines of *U & T (flow variables)* of third-grade nanofluid (Al_2O_3-*SA*) for the variation of third-grade fluid parameter (**Fig. 15 (a)**) and volume fraction (**Fig. 15 (b)**) of nanofluid with coordinates $0 < X < 1,\ 0 < R < 6$. Here, all other parameters are maintained to have constant values such as $\alpha_1 = \alpha_2 = \beta' = 0.001,\ Pr =$

6.2, $GR = 10$, $N = 0.01$ & $M = 0.001$. It may be inferred from **Fig. 15 (a)** that as β amplifies U & T profiles are slightly displaced from the hot cylinder surface. This result is confirmed by the observation that the contour line of U labeled as 1.80 shifts from $R = 5.57$ to 5.77 and the contour line of T labeled as 0.14 as $R\ is\ varied\ from$ 4.18 to 4.25. Similarly, for different values of φ, U and T contour lines migrate and increasingly approach the heated wall (cylinder surface). Here also the T -lines labeled as 0.14 shift from $R = 4.20$ to $R = 4.11$. **Figures 15 (a) & (b)** confirm that the third-grade nanofluid (Al_2O_3-SA) temperature contours are also markedly altered with variation in β and φ values.

5. CONCLUDING REMARKS

A theoretical and computational study has been described to quantify the collective influence of thermal radiation, magnetic field, volume fraction, and geometric shape of nanoparticles on the axisymmetric unsteady convective hydromagnetic boundary layer coating flow of a viscoelastic third-grade nanofluid (Al_2O_3-SA) external to a moving/stationary vertical cylinder. An implicit numerical scheme (Crank Nicolson) has been adopted to solve the transformed, dimensionless nonlinear boundary value problem. Mesh (grid) independence tests and benchmarking with previous simple models from the literature have been included to confirm the accuracy of the numerical code. The influence of key parameters i. e. time (t), Prandtl number (Pr), Grashof number (Gr), radiative flux (N), and third-grade fluid parameter (β). Also, heat transfer characteristics have been analyzed to examine the impact of volume fraction (φ), nanoparticle shape (n), and type of nanoparticle. The key results derived from the study can be summarized as follows:

- Transient velocity and temperature of third-grade nanofluid (Al_2O_3-SA) increase and decreases, respectively with higher volume fractions.
- With the increment in third-grade (viscoelastic) fluid parameter, time-dependent velocity is reduced and temperature is enhanced.

- Steady-state plots (Al_2O_3-*SA*) drawn for moving and stationary cylinders show that heat transfer rates are strongly modified with variation in third-grade fluid parameter.
- Heat transfer characteristics i.e. Nusselt number of Al_2O_3-*SA* increase for higher volume fractions and lower third-grade fluid parameter values.
- The surface skin friction value is augmented for greater volume fraction and smaller third-grade fluid parameter value.
- For higher Grashof number (*Gr*), Prandtl number (Pr) and radiative parameter (N), Nusselt number is boosted.
- Spherical shaped nanoparticles of Al_2O_3-*SA* show a significantly higher thermal performance relative to cylindrical shaped ones.
- Third-grade nanofluid with TiO_2 nanoparticles produces relatively higher heat transfer rates than other nanoparticles (Al_2O_3 and *Cu*).
- Increasing radial magnetic field decelerates the boundary layer flow whereas it elevates temperatures.
- The time taken for both velocity and temperature to attain the steady-state situation is dramatically influenced by viscoelasticity and nanoparticle volume fraction.

As mentioned earlier, the current study has immediate applications in functional (field responsive) magnetic nanomaterial coating dynamics. In particular, Sodium Alginate, a base liquid (third-grade fluid) has significant potential as a biopolymer coating for next generation aerospace and mechanical/chemical components. Additionally, it may have some possible advantages in wound healing biotechnologies [50] and biocompatible, muco-adhesive, and biodegradable polymers [51]. The synthesis of these coating nanomaterials is often conducted at high temperatures wherein thermal radiative effects are appreciable [52] and magnetic induction [53, 54] can arise. However, in such operations, viscous heating i. e. loss of kinetic energy, and furthermore energy losses due to entropy generation may also arise, which have been ignored in the present study, which has also been confined to Boussinesq flows. Future work may consider viscous dissipation, thermodynamic

second law analysis of non-Boussinesq polymer flow of third grade nanofluid [57-61], the porous effect [62], Falkner-Skan flow [63], different non-Newtonian nanofluids [64], [65] and hybrid nanofluids [66], [67] will be communicated soon.

ACKNOWLEDGEMENTS

The authors appreciate greatly the comments of the reviewers which have served to improve the present work.

REFERENCES:

1. H. Masuda, Ebata, A., Teramae, K., and Hishinuma, N. Alteration of thermal conductivity and viscosity of liquid by dispersing ultra-fine particles, *Netsu Bussei*, 7 (4) 227–233 (1993).
2. Yimin Xuan and Qiang Li, Heat transfer enhancement of nanofluids, *International Journal of Heat and Fluid Flow*, 21 (1) 58–64 (2000).
3. Nandy Putra, Wilfried Roetzel and Sarit K. Das, Natural convection of nanofluids, *Heat and Mass Transfer*, 39 (8-9) 775–784 (2003).
4. Elena V Timofeeva, Wenhua Yu, David M France, Dileep Singh and Jules L Routbort, Nanofluids for heat transfer: An engineering approach, *Nanoscale Research Letters*, 6-182 (2011).
5. Wei Yu and Huaqing Xie, A review on nanofluids: preparation, stability mechanisms, and applications, *J. Nanomaterials*, 2012.
6. Wenjea J. Tseng, Chun-Nan Chen**,** Effect of polymeric dispersant on rheological behavior of nickel/terpineol suspensions, *Materials Science and Engineering A*, 347 (2003) 145/153.
7. Wenjea J. Tseng, Kuang-Chih Lin**,** Rheology and colloidal structure of aqueous TiO2 nanoparticle suspensions, *Materials Science and Engineering A*, 355 (2003) 186/192.

8. Kathy lu, Rheological behavior of carbon nanotube-alumina nanoparticle dispersion systems, *Powder Technology*, 177 (3) (2007) 154-161
9. Haisheng Chen, Yulong Ding, Alexei Lapkin, Xiaolei Fan Rheological behaviour of ethylene glycol-titanate nanotube nanofluids, *Journal of Nanoparticle Research*, (2009) 11:1513–1520.
10. Tran X. Phuoc, Mehrdad Massoudi, Experimental observations of the effects of shear rates and particle concentration on the viscosity of Fe2O3–deionized water nanofluids, *International Journal of Thermal Sciences*, 48 (2009) 1294–1301.
11. Haisheng Chen, Yulong Ding, Alexei Lapkin, Rheological behaviour of nanofluids containing tube / rod-like nanoparticles, *Powder Technology*, 194 (2009) 132–141.
12. M. Hojjat, S.Gh. Etemad, R. Bagheri, J. Thibault, Rheological characteristics of non-Newtonian nanofluids: Experimental investigation, *International Communications in Heat and Mass Transfer*, 38 (2011) 144–148.
13. Madhusree Kole T.K. Dey, Viscosity of alumina nanoparticles dispersed in car engine coolant, *Experimental Thermal and Fluid Science*, Volume 34, Issue 6, September 2010, Pages 677-683.
14. N. A. Latiff, M. J. Uddin, O. Anwar Bég and AI. M. Ismail, Unsteady forced bioconvection slip flow of a micropolar nanofluid from a stretching/ shrinking sheet, *Proc. IMechE- Part N: J. Nanomaterials, Nanoengineering and Nanosystems*, 230 (4) pp. 177–187 (2016).
15. P. Rana, R. Bhargava, O. Anwar Bég and A. Kadir, Finite element analysis of viscoelastic nanofluid flow with energy dissipation and internal heat source/sink effects, *Int. J. Applied Computational Mathematics*, 3, 1421–1447 (2017).
16. T. Hayat, M. Z. Kiyani, A. Alsaedi, M. Ijaz Khan and I. Ahmad, Mixed convective three-dimensional flow of Williamson nanofluid subject to chemical reaction, *International Journal of Heat and Mass Transfer*, 127, 422-429 (2018).

17. J. Prakash, E.P. Siva, D Tripathi, S. Kuharat and O. Anwar Bég, Peristaltic pumping of magnetic nanofluids with thermal radiation and temperature-dependent viscosity effects: modelling a solar magneto-biomimetic nanopump, *Renewable Energy* (2018). 18 pages. doi.org/10.1016/j.renene.2018.08.096 0960-1481
18. M. J. Uddin, O. Anwar Bég, P. K. Ghose and A.I.M. Ismael, Numerical study of non-Newtonian nanofluid transport in a porous medium with multiple convective boundary conditions and nonlinear thermal radiation effects, *Int. J. Num. Meth. Heat Fluid Flow*, 26 (5) 1-25 (2016).
19. R.L. Fosdick and K.R. Rajagopal, Thermodynamics and stability of fluids of third-grade, *Proc. Royal Society of London. Series A*, 369 351 – 377 (1980).
20. R. Byron Bird, Robert C. Armstrong, Ole Hassager, *Dynamics of Polymeric Liquids, Volume 1: Fluid Mechanics*, 2nd Edition, Wiley USA (1987).
21. T. Javed and I. Mustafa, Slip effects on a mixed convection flow of a third-grade fluid near the orthogonal stagnation point on a vertical surface, *J. Applied Mechanics and Technical Physics*, 57, 527–536 (2016).
22. O. Anwar Bég, H. S. Takhar, R. Bhargava, S. Rawat and V. R. Prasad, Numerical study of heat transfer of a third-grade viscoelastic fluid in a non-Darcy porous media with thermophysical effects, *Physica Scripta*, 77 (2008) 065402-13.
23. G. J. Reddy, A. Hiremath, and M. Kumar, Computational modeling of unsteady third-grade fluid flow over a vertical cylinder: a study of heat transfer visualization, *Results in Physics*, 8 671-682 (2018).
24. G. J. Reddy, A. Hiremath, Hussain Basha and N. S. Venkata Narayanan, Transient flow and heat transfer characteristics of non-Newtonian supercritical third-grade fluid (CO_2) past a vertical cylinder, *International Journal of Chemical Reactor Engineering*, 20170232 (2018).

25. A. Hiremath, G. J. Reddy, M. Kumar and O. Anwar Bég, Unsteady free convective heat transfer in third-grade fluid flow from an isothermal vertical plate: A thermodynamic analysis, *International Journal of Modern Physics B*, 33, (08) 1950060 (2019).
26. A. Hiremath and G. J. Reddy Transient analysis of third-grade fluid flow past a vertical cylinder embedded in a porous medium, *Numerical Heat Transfer and Fluid Flow, Lecture Notes in Mechanical Engineering*, 83-91 (2019).
27. A. Hiremath, G. J. Reddy and O. Anwar Bég, Computational unsteady flow analysis for third-grade fluid from an isothermal vertical cylinder through a Darcian porous medium, *Heat Transfer*, 48 (7), 2752-2772 (2019).
28. A. Hiremath, G. J. Reddy and O. Anwar Bég, Transient analysis of third-grade viscoelastic nanofluid flow external to a heated cylinder with buoyancy effects, *Arabian Journal for Science and Engineering*, 44, 7875–7893 (2019).
29. U. Farooq, T. Hayat, A. Alsaedi and S. Liao, Heat and mass transfer of two-layer flows of third-grade nano-fluids in a vertical channel, *Applied Math. Comp*., 242 528-540 (2014).
30. S. Nadeem and S. Saleem, Analytical study of third-grade fluid over a rotating vertical cone in the presence of nanoparticles, *Int. J. Heat Mass Transfer*, 85 1041-1048 (2015).
31. W. A. Khan, J. R. Culham and O. D. Makinde, Combined heat and mass transfer of third-grade nanofluids over a convectively-heated stretching permeable surface, *Canadian Journal of Chemical Engineering*, 93 1880-1888 (2015).
32. S. Qayyum, T. Hayat and A. Alsaedi, Thermal radiation and heat generation/absorption aspects in third-grade magneto-nanofluid over a slendering stretching sheet with Newtonian conditions, *Physica B: Condensed Matter*, 537 139–149 (2018).
33. T. Hayat, S. Ahmad, M. Ijaz Khan and A. Alsaedi, Modeling and analyzing flow of third-grade nanofluid due to rotating stretchable disk with chemical reaction and heat source, *Physica B: Condensed Matter*, 537 116–126 (2018).

34. V. Rajesh, A.J. Chamkha, Ch. Sridevi, A.F. Al-Mudhaf, A numerical investigation of transient MHD free convective flow of a nanofluid over a moving semi-infinite vertical cylinder, *Engineering Computations*, 34 (5), (2017) 1393-1412.
35. V. Rajesh, O. Anwar Bég and Ch. Sridevi, Finite difference analysis of unsteady MHD free convective flow over moving semi-infinite vertical cylinder with chemical reaction and temperature oscillation effects, *Journal of Applied Fluid Mechanics*, 9(1) (2016), 157-167.
36. B. Mahanthesh, B. J. Gireesha, Rama Subba Reddy Gorla, Heat and Mass transfer effect on the mixed convective flow of chemically reacting nanofluid past a moving/stationary vertical plate, *Alexandria Engineering Journal*, 55 (2016), 569-581.
37. I. Tlili, W.A. Khan, I. Khan, Multiple slips effects on MHD SA-Al2O3 and SA-Cu non-Newtonian nanofluids flow over a stretching cylinder in porous medium with radiation and chemical reaction, *Results in Physics*, 8 (2018) 213–222
38. S.S. Pawar, Vivek K. Sunnapwar, Experimental studies on heat transfer to Newtonian and non-Newtonian fluids in helical coils with laminar and turbulent flow, *Experimental Thermal and Fluid Science*, 44 (2013) 792–804
39. M. Hatami, D.D. Ganji, Heat transfer and flow analysis for SA-TiO_2 non-Newtonian nanoflui passing through the porous media between two coaxial cylinders, Journal of Molecular Liquids 188 (2013) 155–161.
40. Arshad Khan, Dolat Khan, Ilyas Khan, Farhad Ali, Faizan ul Karim & Muhammad Imran, MHD flow of sodium alginate based casson type nanofuid passing through a porous medium with newtonian heating, *Scientific Reports* 8 (2018) 8645.
41. M. Hojjat, S.Gh. Etemad, R. Bagheri, J. Thibault, Thermal conductivity of non-Newtonian nanofluids: Experimental data and modeling using neural network, *Int. J. Heat Mass Transfer*, 54 (2011) 1017-1023.

42. Tarek Nabil Ahmed, Ilyas Khan, Mixed convection flow of sodium alginate (SA-NaAlg) based molybdenum disulphide (MoS2) nanofluids: Maxwell-Garnett and Brinkman models, *Results in Physics* 8 (2018) 752–757.
43. Tiwari R. K. and Das M. K, Heat transfer augmentation in a two-sided lid-driven differentially heated square cavity utilizing nanofluids. *Int J Heat Mass Transfer*, 50(9–10) (2007), 2002–2018.
44. Schlichting H and Gersten K., *Boundary Layer Theory*. New York: Springer-Verlag, 2001.
45. Hamilton R. L. and Crosser O. K, Thermal conductivity of heterogeneous two component system. *Ind Eng Chem Fund*, 1 (1962) 187–191.
46. Brewster MQ, *Thermal Radiative Transfer and Properties*, John Wiley & Sons, New York, 1992.
47. Carnahan B, Luther HA and Wilkes JO. *Applied Numerical Methods*. New York: John Wiley & Sons, 1969.
48. Von Rosenberg DU, *Methods for the Numerical Solution of Partial Differential Equations*, American Elsevier Publishing Company, New York (1969).
49. H. P. Rani and C. N. Kim, Transient convection on a vertical cylinder with variable viscosity and thermal conductivity, *AIAA J. Thermophysics Heat Transfer*, 22 (2008) 254-261.
50. M. Aneja, Sapna Sharma, S. Kuharat and O. Anwar Bég, Computation of electroconductive gyrotactic bioconvection under nonuniform magnetic field: Simulation of smart bio-nanopolymer coatings for solar energy, *Int. J. Modern Physics B,* 33, 2050028 (22 pages). (2020)**.**
51. Ioannis Liakos, Loris Rizzello, David J. Scurr, Pier Paolo Pompa, Ilker S. Bayer, Athanassia Athanassiou, All-natural composite wound dressing films of essential oils encapsulated in sodium alginate with antimicrobial properties, *International Journal of Pharmaceutics* 463(2) (2014) 137-45.
52. Chang H and Chang Y-C. Fabrication of Al_2O_3 nanofluid by a plasma arc nanoparticles synthesis system. *J Mater Process Tech.*, 2008; 207(1–3): 193–199.

53. O. Anwar Bég, S. Kuharat, M. Ferdows, M. Das, A. Kadir, M. Shamshuddin, Magnetic nano-polymer flow with magnetic induction and nanoparticle solid volume fraction effects: *solar magnetic nano-polymer fabrication simulation, Proc. IMechE-Part N: J Nanoengineering, Nanomaterials and Nano-systems* (2019). DOI: 10.1177/ 2397791419838714 (19 pages)
54. M.M. Bhatti, C.M. Khalique, Tasveer Bég, O. Anwar Bég and Ali Kadir, Numerical study of slip and radiative effects on magnetic Fe_3O_4-water-based nanofluid flow from a nonlinear stretching sheet in porous media with Soret and Dufour diffusion, *Modern Physics Letters B*, 33, 2050026 (24 pages) (2020).
55. Dunn, J. E. and Rajagopal, K. R. Fluids of differential type: critical review and thermodynamic analysis, International Journal of Engineering Science, 33, 689 - 729 (1995).
56. R. L. Fosdick and B. Straughan, Catastrophic instabilities and related results in a fluid of third grade. Int. J. Non-Linear Mech., 16, 191 (1981).
57. Mubbashar Nazeer, M. Ijaz Khan, Yu-Ming Chu, Seifedine Kadry & Mohamed R. Eid, Mathematical modeling of multiphase flows of third-grade fluid with lubrication effects through an inclined channel: analytical treatment, Journal of Dispersion Science and Technology, (2021).
58. Sihem Lahmar, Mohamed Kezzar, Mohamed R. Eid and Mohamed Rafik Sari, Heat transfer of squeezing unsteady nanofluid flow under the effects of an inclined magnetic field and variable thermal conductivity, Physica A (2019).
59. Ahcene Nouar, Amar Dib, Mohamed Kezzar, Mohamed R. Sari and Mohamed R. Eid, Numerical treatment of squeezing unsteady nanofluid flow using optimized stochastic algorithm, Zeitschrift für Naturforschung A, (2021).
60. Abderrahim Wakif, Zoubair Boulahia, Farhad Ali, Mohamed R. Eid & Rachid Sehaqui, Numerical analysis of the unsteady natural convection MHD Couette nanofluid flow in the presence of thermal radiation using single and two-phase nanofluid models for Cu–Water nanofluids, International Journal of Applied and Computational Mathematics, 4, 81 (2018).
61. Mohamed R. Eid and Kasseb L. Mahny, Unsteady MHD heat and mass transfer of a non-Newtonian nanofluid flow of a two-phase model over a permeable stretching wall with heat generation/absorption, Advanced Powder Technology, 28(11), pp. 3063-3073, (2017).
62. Mohamed R. Eid, A. F. Al-Hossainy, and M. Sh. Zoromba, FEM for blood-based SWCNTs flow through a circular cylinder in a porous medium with electromagnetic radiation, Communications in Theoretical Physics, 71, 1425, (2019).

63. Nawel Boumaiza, Mohamed Kezzar, Mohamed R. Eid, and Ismail Tabet, On numerical and analytical solutions for mixed convection Falkner-Skan flow of nanofluids with variable thermal conductivity, Waves in Random and Complex Media, (2019).
64. Wasim Jamshed, Faisal Shahza, Rabia Safdar, Tanveer Sajid, Mohamed R. Eid, and Kottakkaran Sooppy Nisar, Implementing renewable solar energy in presence of Maxwell nanofluid in parabolic trough solar collector: a computational study, Waves in Random and Complex Media, (2021).
65. Hassan Waqas, Mohib Hussain, M. S. Alqarni, Mohamed R. Eid, and Taseer Muhammad, Numerical simulation for magnetic dipole in bioconvection flow of Jeffrey nanofluid with swimming motile microorganisms, Waves in Random and Complex Media, (2021).
66. Ahmed F. Al-Hossainy and Mohamed R. Eid, Combined theoretical and experimental DFT-TDDFT and thermal characteristics of 3-D flow in rotating tube of [PEG + H_2O/SiO_2-Fe_3O_4]^C hybrid nanofluid to enhancing oil extraction, Waves in Random and Complex Media, (2021).
67. Mohamed R. Eid and Ahmed F. Al-Hossainy, Combined experimental thin film, DFT-TDDFT computational study, flow and heat transfer in [PG-MoS_2/ZrO_2]^C hybrid nanofluid, Waves in Random and Complex Media, (2021).